Title

Environmental and Economic Impacts of Managing Nutrients in Digestate Derived from Sewage Sludge and High-Strength Organic Waste

Journal

Environmental Science and Technology, 56(23)

ISSN

0013-936X

Authors

Orner, Kevin D

Smith, Sarah

Nordahl, Sarah

et al.

Publication Date

2022-12-06

DOI

10.1021/acs.est.2c04020

Formation, cooling history and age of impact events on the IIE iron parent body: evidence from the Miles meteorite

Rachel S. Kirby[1,*], Penelope L. King[1], Marc D. Norman[1], Trevor R. Ireland[1,#], Margaret Forster[1], Arthur D. Pelton[2], Ulrike Troitzsch[1], Nobumichi Tamura[3]

[1] Research School of Earth Sciences, The Australian National University, Acton ACT 2601, Australia

[2] Center for Research in Computational Thermochemistry, Department of Chemical Engineering, Polytechnique Montréal, Montréal QC H3T 1J4 Canada

[3] Advanced Light Source, Lawrence Berkeley National Laboratory, 1 Cyclotron Road, Berkeley, CA 94720, U.S.A.

*Corresponding Author: Rachel S. Kirby, rachel.kirby@anu.edu.au

[#] School of Earth and Environmental Sciences, The University of Queensland, Brisbane QLD 4072, Australia *(present address)*

ABSTRACT

Most iron meteorites formed in planetary cores during differentiation, but the IIE iron meteorites have chemical and physical features that are inconsistent with this origin. By combining mineral chemistry, mineral modes and three-dimensional petrography, we reconstruct the bulk chemistry of the felsic silicate-bearing Miles IIE iron meteorite and demonstrate that the silicate inclusion compositions are similar to partial melts produced experimentally from an H chondrite composition. We use the reconstructed bulk composition, mineralogy and thermodynamic modelling to show that melting above ~1200 °C under reducing conditions formed metal (Fe-Ni alloy) and felsic silicate partial melts. Upon cooling, the melts crystallized Mg-rich pyroxenes, Na- and K-rich feldspars, and tridymite. Importantly, this mechanism enriches cosmochemically volatile elements (i.e., those with a 50% condensation temperature of ~430-830 °C, like Na and K) to the level found in the felsic silicate inclusions.

The presence of crystallographically disordered srilankite (only stable above 1160 °C) and an absence of Widmanstätten texture require both high peak temperatures and rapid cooling, which cannot be explained by core formation Instead they point to small melt volumes, a transient heat pulse, and small thermal mass, and imply efficient physical segregation of silicate and metallic melts through buoyancy separation followed by rapid cooling that arrested the separation of metal and silicate liquid phases. In situ $^{207}Pb/^{206}Pb$ ages of 4542 ± 4.0 Ma in Zr-oxide minerals determined here date the melting event that formed the silicate inclusions. This age aligns with the earliest ages found in other IIE iron meteorite silicates and requires a heating event ~25 million years after the solar system formed. We found $^{39}Ar/^{40}Ar$ ages of 3495 ± 52 Ma (low-T) and 4303 ± 7 Ma (high-T) in a K-feldspar grain, with the 3495 Ma age aligning with later thermal events recorded in other IIE iron meteorites. Dating reveals the complex petrogenetic and thermal history of Miles and the IIE iron meteorites. This is the first IIE iron meteorite found to record evidence of impact bombardment at 4.5 and 3.5 Ga.

High-velocity impact(s) into an iron-rich, porous chondritic parent body at ~4.54 Ga produced immiscible metal and silicate melts that cooled rapidly and trapped low density silicate inclusions within high density metal. Other IIE irons that formed at lower peak temperatures (900-1000 °C) contain chondritic silicate inclusions and relict chondrules, supporting this conceptual model. Our model is consistent with thermodynamic modelling, experimental data and the wide range of peak temperatures and cooling rates observed in the IIE iron meteorites.

Keywords

IIE iron meteorites; silicate inclusions; impact melting; partial melting; geochronology

1. INTRODUCTION

Most iron meteorites formed in the cores of planetary bodies in the early solar system (Chabot and Haack, 2006). In contrast, IIE iron meteorites have an unusual petrography with abundant feldspar-

bearing inclusions that are more typical of a planetary crust (Bunch et al., 1970; Armstrong et al., 1990; Ruzicka et al., 1999; Hsu, 2003). These mineral assemblages indicate high formation temperatures (>1000°C; e.g. Ruzicka and Hutson 2010) even though the silicate inclusions have abundant cosmochemically volatile elements with 50% condensation temperatures <830 °C (e.g., Na and K; Lodders, 2003). In addition, the IIEs do not show evidence of fractional crystallisation of a metallic liquid in the core of large parent bodies in their Ni, Ir, Ge and/or Ga contents (e.g., Scott and Wasson, 1975; Chabot and Haack, 2006; Goldstein et al., 2009). These petrographic and geochemical features cannot be explained by simple models of core formation. Current hypotheses for the formation of IIE iron meteorites include 1) impact events that mixed differentiated or partially differentiated materials (e.g., Ruzicka, 2014; McDermott et al., 2016); 2) impact events that melted chondritic materials (e.g., Wasson, 2017); 3) extreme planetary differentiation (Wasserburg et al., 1968; McCoy, 1995); and, 4) subsolidus condensation and metasomatism (Kurat et al., 2007).

Any hypothesis for the formation of the IIE iron meteorites must account for the diverse mineralogical, geochemical and petrological features of the group. The 25 known meteorites in the IIE iron group have a range of lithologies: some contain chondritic silicate inclusions with H chondrite-like clasts and chondrules (e.g. Netschaëvo; Bunch et al., 1970); some only contain metal (e.g. Arlington; Buchwald, 1975); and others contain felsic silicate inclusions (e.g. Miles; Ikeda and Prinz, 1996). Inclusions containing primarily olivine, orthopyroxene and feldspar with a roughly chondritic bulk composition are found in Watson 001 (Bogard et al., 2000); chondritic inclusions are also found alongside H chondrite-like clasts and relict chondrules in Netschaëvo (Bunch et al., 1970; Olsen and Jarosewich, 1971; Bild and Wasson, 1977) and an unmelted H chondrite inclusion in Techado (Casanova et al., 1995). Mont Dieu (iron-ungrouped) has been linked to IIE and it contains H chondrite like clasts and relict chondrules (Van Roosbroek et al., 2015). Felsic inclusions, consisting predominantly of albite, Si-rich glass, tridymite, and K-feldspar, with little to no olivine, are found in

73 Miles, Weekeroo Station, Colomera, Kodaikanal, Elga, Tarahumara and Taylor Glacier 05181
74 (Ruzicka, 2014).

75 Peak temperatures for the IIE irons with chondritic inclusions are 920 – 1080°C for Netschaëvo and
76 Mont Dieu (Van Roosbroek et al., 2015), with Watson 001 recording brief, local heating to >700°C
77 (Bogard et al., 2000). In comparison, peak temperatures for the IIE irons with silicate inclusions are
78 1250°C (Miles; Ruzicka and Hutson, 2010). A range of cooling rates is indicated by metallographic
79 textures (Scott and Wasson, 1976). For example, Miles cooled quickly (100-10 000˚C/Myr; Goldstein
80 et al., 2009) as no Widmanstätten pattern has developed in the metal (Ikeda et al., 1997). In
81 contrast, the metal in some of the other IIE iron meteorites such as Arlington and Weekeroo Station
82 contain Widmanstätten textures (Buchwald, 1975), implying slower cooling rates.

83 Two distinct age groups are identified at ~4.5 Ga and ~3.6 Ga, but these age groups do not align with
84 meteorite petrography (i.e., chondritic silicate-bearing, silicate-free, and felsic silicate-bearing;
85 Ruzicka, 2014), nor with the cooling rates. Despite extensive studies, no single formation model has
86 adequately addressed the range in peak temperatures, cooling rates, silicate chemistry and ages
87 experienced across the IIE iron meteorite group in the context of a heating event >20 Myr after CAI
88 formation at 4.567 Ga (Connelly et al., 2012). These features, along with the low oxygen fugacity
89 conditions and coexistence of phases with vastly different densities (i.e., metal and silicates), remain
90 to be explained.

91 To test the multiple hypotheses for IIE iron meteorite formation we studied Miles because it appears
92 to preserve important primary features of the formation event. Specifically, Miles: 1) cooled quickly
93 as shown by an absence of Widmanstätten pattern (Ikeda et al., 1997); 2) a bulk silicate inclusion has
94 been dated to 4.408 ± 0.009 Ga (Ar-Ar; Bogard et al., 2000) therefore is less likely to have been
95 altered by later thermal event(s); and, 3) it contains abundant felsic silicate inclusions (Ikeda et al.,
96 1997). We apply two- and three-dimensional geochemistry, mineralogy and petrography of the
97 Miles meteorite as a basis for investigating the different hypotheses of formation. We calculate peak

temperatures and cooling rates for Miles along with ^{207}Pb-^{206}Pb isotopic and Ar-Ar ages to investigate it's thermal history. We evaluate the geochemistry and chemical reactions that determine the conditions required to form Miles. We apply physical and thermodynamic models to unravel the process of formation and physical segregation of silicate and metallic melt. Finally, we apply our approaches with the Miles meteorite to the IIE iron meteorite group and resolve ambiguities in the previous geochronology with implications for petrogenesis and thermal history.

2. MATERIALS AND METHODS

2.1 Sample selection and preparation

For this study a 4 x 2 x 2 cm sawn sample of Miles loaned from the private collection of Richard Arculus was cut into subsections and polished without water to avoid alteration or removal of water-soluble phases. Prior to Scanning Electron Microscopy (SEM), subsections RA1, RA2, and RA4 were coated with ~12 nm of carbon. Prior to analysis on SHRIMP (Sensitive High Resolution Ion Microprobe), subsections RA1 and RA2 were cleaned and coated with ~30 nm evaporated gold.

2.2 Petrographic and mineralogic analyses

2.2.1. Micro-X-ray Computed Tomography

Subsection RA4 (15 x 8 x 5 mm) was imaged using micro-X-ray computed tomography (μCT) at the CTLab in the Department of Applied Mathematics, Research School of Physics (ANU). This sample was selected due to its appropriate diameter which allows the attenuation of x-rays through the relatively dense metal. Results were compared to the 2D analysis of the larger sample to ensure that a) the volume of silicate:metal in the smaller sample was the same as the exposed silicate:metal in the larger sample; and b) that it visually appeared to be representative of the larger sample. An X-ray source with an accelerating voltage of 150 keV and a beam current of 109 A was used. The sample was moved along a double-helix trajectory with 2520 radiographs taken per revolution on a

Varian Flat Panel camera detector. A tomogram with a 7µm voxel size was created with 11,190 radiographs using the software package Drishti-2 (Limaye, 2012).

2.2.2 Scanning Electron Microscopy

Scanning electron microscopy was conducted at the Centre of Advanced Microscopy (CAM), ANU and included imaging and qualitative phase identification. For quantitative major element chemistry of phases, the following instruments were used with operating conditions given in parentheses (accelerating voltage, probe current and working distance): a JEOL JSM6400 with an Oxford ISIS 350 Energy Dispersive X-Ray Analysis (EDXA) system (10 kV, 0.6nA, 29mm), a Hitachi 4300 SE/N Schottky Field Emission SEM (FESEM) with an INCA Energy EDXA system (15kV, 6nA, 25mm), and a Zeiss UltraPlus analytical FESEM with an INCA Energy 450 EDXA system (10kV, 1nA, 11mm). We considered results acceptable for quantitative analysis when both the live time was ≥ 60s and the totals fell between 98 wt.% and 102 wt.%. The EDXA systems were externally calibrated using mineral standards at CAM and matrix corrections from ZAF factors (Z = atomic number effects, A = absorption of X-rays, and F = X-ray fluorescence) were applied. Instrument use was subject to availability and the use of different SEMs did not impact on results.

The total exposed area of each phase was measured on 22 of the silicate inclusions including all of the inclusions in RA4A and 18 of the 21 inclusions in RA1A to eliminate selection bias. We used the wt.% from area exposed plus the average major element chemistry to estimate the bulk chemistry of each silicate inclusion, assuming the area exposed was the same as the volume. Inclusion i21 was excluded from these estimates due to its extremely anomalous composition – a full description of this inclusion is available in the Supplement. Analyses of the areas of phases exposed on the surface was conducted using the USA National Institute of Health ImageJ software.

2.2.3 Micro-scanning X-ray diffraction

Micro-scanning X-ray diffraction (µSXRD) analyses were conducted using synchrotron beamline 12.3.2 at the Advanced Light Source, Lawrence Berkeley National Laboratory (Tamura et al., 2009).

Samples were mounted on an xyz stage at a 45^{o} angle with respect to the beam, and raster scanned with a polychromatic beam (6-22 keV) of about 1 µm x 1 µm in size, with 2 µm step size. A Laue pattern was collected at each step with a 2 second exposure using an X-ray area detector (DECTRIS Pilatus 1M) mounted vertically at a distance of approximately 150 mm above the samples. The Laue diffraction patterns were indexed for phase identification using the software XMAS (Tamura, 2014).

2.3 U-Th-Pb isotopes

U-Th-Pb isotopes were measured on individual grains of srilankite, zirconolite, baddeleyite, chlorapatite and merrillite in three silicate inclusions (i29, i11, and i7) using the SHRIMP-RG (Sensitive High Resolution Ion Microprobe – Reverse Geometry) at the Research School of Earth Sciences (RSES), ANU following standard operating procedures (Ireland and Williams, 2003; Ireland et al., 2008).

The sample was sputtered with a primary O_2^- beam, with primary and extraction accelerating voltages of 10 kV. A 10 µm diameter beam was used for analysis of the small srilankite ($ZrTi_2O_6$) and zirconolite ($CaZrTi_2O_7$), and baddeleyite (ZrO_2) grains, whereas a 30 µm diameter beam was used for the larger phosphate minerals to increase sensitivity. Mass spectra were obtained for the individual mineral phases and demonstrated no significant interferences at the operating mass resolution of 5000 M/ΔM (1% peak height).

The masses analyzed through the run table included $^{196}(Zr_2O)^+$, $^{204}Pb^+$, $^{206}Pb^+$, $^{207}Pb^+$, $^{208}Pb^+$, $^{238}U^+$, $^{248}ThO^+$, and $^{254}UO^+$. In addition, a background was measured at mass 204.1. Integration time per cycle was 2 seconds for ^{196}Zr and ^{248}ThO, 3s for ^{254}UO, 5s for ^{208}Pb and ^{238}U, and 10 seconds each for ^{204}Pb, ^{206}Pb, ^{207}Pb, ^{208}Pb, and background.

Zirconium is present in srilankite, zirconolite and baddeleyite and so the $^{196}Zr_2O^+$ was used to monitor peak drift for these phases. In addition, we reanalyzed grain RA1A-Zirk-1, which has a high concentration of Zr, U and Pb. Analysis of the phosphates used the same run table. No mineral

standards were available for srilankite and zirconolite, while baddeleyite may be calibrated to zircon. SL13 and FC1 zircon standards were analyzed during the course of this work to maintain peak positions and verify data.

Data were reduced with the in-house SQUID 2.0 data reduction program. For this work, no calibrated U-Pb age was determined, although the Pb/U data and apparent U concentration (via countrate) is used to evaluate likely concordance. Common-Pb corrections were applied using $^{204}Pb/^{206}Pb$ assuming a Canyon Diablo Troilite initial Pb isotope composition.

A semiquantitative U concentration estimate may be made based on a direct comparison of $^{238}U^{+}$ count rate referenced to the SL13 zircon standard ([U] = 238 ppm; [Th] = 20 ppm), referred to below as apparent concentrations. There is a potential for a matrix effect between these different mineral phases, but this bias may be relatively small because they are all zirconium based oxides/silicates.

2.4 $^{39}Ar/^{40}Ar$ dating

A clean single K-feldspar grain (identity confirmed by optical and scanning microscopy, and micro-reflectance infrared spectroscopy) was irradiated at The McClellan Nuclear Research Center, University of California Davis, USA, in the Christiansen feature (CF) position for 30.0MWh. This grain and accompanying standards were analyzed for Ar isotopic compositions at RSES, ANU (see below). The canister used in the irradiation had a 1.0 mm cadmium lining for shielding from slow neutrons. The flux monitor used was GA1550 assuming an age of 98.5 ±0.8 Ma (Spell and McDougall, 2003). The salts CaF_2 and zero-age K-glass were also irradiated and the following results were obtained: ($^{36}Ar/^{37}Ar$) Ca correction factor 2.23^{E-04}; ($^{39}Ar/^{37}Ar$) Ca correction factor 6.33^{E-04}; ($^{40}Ar/^{39}Ar$) K correction factor 1.34^{E-02}; ($^{38}Ar/^{39}Ar$) K correction factor 1.16^{E-02}; (^{38}Ar) Cl/ (^{39}Ar) K correction factor 8.23^{E-02}; Average J=5.68059^{E-3}; (J/MWh = 1.89353^{E-4}; Ca/K conversion factor 1.90; $\lambda^{40}K$ 5.5430^{E-10} was used. Ages were calculated using the ^{40}K abundances and decay constants of Steiger and Jäger (1977).

194 The Ar isotopic data were obtained using the diffusion, step-heating furnace technique (Forster and
195 Lister, 2009). The analyses were conducted with a double-vacuum resistance furnace for gas
196 extraction and the single collector VG1200 gas source mass spectrometer. Samples were dropped
197 into the furnace for 12 hours prior to analysis, leaving them at a 400°C, with a 2-minute pulse up to
198 420°C, or 30°C below the starting temperature (450°C). Any gas released during the pre-heating
199 stage was pumped away prior to analysis to minimize gas contamination. Samples were
200 incrementally heated in a manner to optimize the gas release as evenly as possible until fusion (at
201 1450°C).

202 The raw data were reduced using the software Noble v1.8 (version adapted 2016). The measured Ar
203 isotope concentrations are displayed for each heating step in the Supplement, with uncertainties in
204 isotopic ratios and ages at quoted 2σ SD level. Weighted mean ages and uncertainties were
205 calculated using the eArgon software (written by G. Lister) and interpreted using the Asymptote and
206 Limits method (Forster and Lister, 2004).

207 # 3. RESULTS

208 ## *3.1 Petrography and mineralogy*

209 X-ray micro computed tomography shows that the 600 mm^3 sample RA4 consists of 80 vol.% metal
210 and 20 vol.% silicate + phosphate inclusions (hereafter referred to as silicate inclusions). These
211 inclusions are found at the junctions of Fe-Ni metal grains, identified by Wasson (2017) as parental
212 γ-grains (Fig. 1 A-C). The metal is predominantly kamacite (92 wt.% Fe, 7 wt.% Ni) with minor
213 irregularly shaped taenite (60-75 wt.% Fe, 25-40 wt.% Ni) grains (Ikeda and Prinz, 1996). The
214 kamacite grains are less than 1 cm across and form triple-junction boundaries (Fig. 1 B, C). We did
215 not observe a Widmanstätten pattern in the metal, consistent with Ruzicka (2014). Schreibersite
216 [$(Fe,Ni)_3P$] makes up ~3.2% and troilite [FeS] <1% of the metal by area. Schreibersite is concentrated
217 along the margins of the metal grain boundaries and less commonly occurs adjacent to the silicate

inclusions (Fig. 1C). In rare cases, the metal grain boundaries contain secondary minerals (e.g., hematite, goethite, kaolinite, collinsite), likely due to terrestrial weathering.

Figure 1 near here

Silicate inclusions are 3 to 30 mm in length, with the majority irregular and globular in shape. Some of the inclusions are elongate and appear to follow metal grain boundaries as shown in the 2D and 3D images (Fig. 1). Inclusions are aggregates of silicates + phosphates + oxides with only a few containing grains of metal, schreibersite and/or troilite (Table 1). The boundary between the metal and silicate inclusions is frequently cuspate (Fig. 1B-D) forming an overall globular shape to the inclusions.

Table 1 near here

The mineralogy of each inclusion studied here is summarized in Table 1. Within the inclusions, augite ($En_{47-51}Fs_{8-11}Wo_{37-45}$; Table 2 for analyses) and enstatite ($En_{68-91}Fs_{7-28}Wo_{2-4}$) are commonly partially or fully enclosed by albite ($Ab_{93}An_4Or_3$). K-feldspar ($An_1Ab_{10}Or_{88-100}$) is typically confined to the margins of the inclusions. Phosphates are always associated with silicates and commonly occur as lobes extending from the margins of inclusions (Fig. 1B-D). Cr-spinel occurs as euhedral crystals associated with pyroxenes (Fig. 1D). Inverted pigeonite is present as augite + enstatite lamellae. Tridymite (confirmed by synchrotron micro-XRD) predominantly occurs as globular features interspersed with other minerals such as chlorapatite, albite, and intergrown K-feldspar + albite (Fig. 1D). In one inclusion tridymite occurs as lamellae with K-feldspar and albite (Fig. 2C) and in another these minerals have formed a micrographic texture (Fig. 2D). The 2-feldspar ± tridymite lamellae is associated with Zr- and Ti-bearing oxide minerals (Fig. 2B,C). Oxide minerals found in Miles silicate inclusions include rutile, disordered srilankite (verified by synchrotron micro-XRD), baddeleyite, ilmenite-geikielite, ferropseudobrookite, and two zirconolite-like minerals, one containing 3.22 wt.% Th (Table 1).

Table 2 near here

Silicate inclusions are subdivided into three main groups based on their silicate mineralogy. Type A inclusions are composed of albite + (augite and/or enstatite), Type B of albite + augite + (K-feldspar and/or tridymite) ± enstatite (Fig. 1D), and Type C of albite + K-feldspar + tridymite (Table 1; Fig. 2). Type A inclusions are the most abundant and comprise approximately 50% of the exposed area of inclusions. About 45% of the inclusions by area are Type B, with ~5% Type C. Type C inclusions are distinct from Type A and B because they contain no pyroxene, have high silica contents and are enriched in incompatible elements. There is one anomalous inclusion: this is described in more detail in the Supplement.

Figure 2 near here

3.2 Major element chemistry

The estimated bulk composition of all inclusions weighted by area exposed for SEM analysis (excluding the anomalous inclusion i21; Supplement) is 60 wt.% SiO_2, 10 wt.% Al_2O_3, 4 wt.% FeO, 10 wt.% MgO, 9 wt.% CaO, and 5 wt.% Na_2O_3 (Table 3). These estimates were obtained using the mineral area analyses of each inclusion (Table 1), estimated mineral densities (Table 3 notes), and the average major element chemistry for each mineral (Table 2). The estimated bulk composition of each inclusion depends on the proportion of the minerals exposed, for example inclusion i11 consists predominantly of tridymite + K-feldspar + albite (Table 1) and therefore has anomalously high SiO_2 and K_2O contents (Table 3).

Table 3 near here

3.3. U-Th-Pb and $^{207}Pb/^{206}Pb$ Geochronology

U-Th-Pb isotopes were measured on zirconolite, srilankite, baddeleyite and chlorapatite grains. The variability of $^{206}Pb/^{238}U$ of the srilankite analyses is quite low (approximately 10%) which suggests that the ^{206}Pb is likely radiogenic. This is further supported by low values of $^{204}Pb/^{206}Pb$ of $<5x10^{-5}$ ($^{206}Pb/^{204}Pb$ of >20,000) for srilankite indicating initial Pb is not a strong influence on $^{207}Pb/^{206}Pb$

ages. The $^{207}Pb/^{206}Pb$ of the srilankite analyses are remarkably uniform with ages ranging from 4541 ± 3 to 4544 ± 4 Ma (1σ). For zirconolite, two analyses have low $^{204}Pb/^{206}Pb$, however Zirk-2A has substantially higher $^{204}Pb/^{206}Pb$ at ca. 10^{-2} and has a large uncertainty. This uncertainty seems to correlate with the apparent U concentrations in these analyses (high U in Zirk-1 and low U in Zirk-2). Of the zirconolite analyses, only Zirk-1 has high U and has a comparable uncertainty of 4539 ± 6 Ma. The remaining analyses of zirconolite, baddeleyite, and chlorapatite are consistent with these values, but with large uncertainties. Baddeleyite and chlorapatite have high $^{204}Pb/^{206}Pb$ largely because of their low U contents and higher contributions of common Pb.

The mean of all analyses provides a $^{207}Pb/^{206}Pb$ age of 4542.3 ± 4.0 Ma ($2\sigma_m$; n=9/9; MSWD = 0.42; Table 4). The weighted mean is dominated by the srilankite analyses, which have the highest U and ^{206}Pb concentrations and hence the highest precision in $^{207}Pb/^{206}Pb$. If only the srilankite analyses are considered, the mean $^{207}Pb/^{206}Pb$ age is 4543 ± 4 ($2\sigma_m$; n=3/9; MSWD = 0.34). The formation age of the Miles meteorite is taken as the weighted mean of all analyses to account for the high errors on some measurements (i.e., 4542.3 ± 4.0 Ma).

Table 4 near here

3.4 ^{40}Ar-^{39}Ar Geochronology

The gas release spectra obtained from the K-feldspar grain shows clear evidence for low-T diffusive loss, and two distinct partial plateaus corresponding to ages of 3495 ± 52 Ma (low-T) and 4303 ± 7 Ma (high-T) (Fig. 3). The K/Ca ratios at these partial plateaus was mostly less than 1, within the acceptable range for K-feldspar. The younger age segment consisted of four steps and accounts for 22% of the released gas, whereas the older segment consisted of three steps and accounts for 18% of the gas release.

Figure 3 near here

290 # 4. DISCUSSION

291 ## *4.1 Petrogenetic context for the thermal and redox history of Miles*

292 The petrography of the Miles meteorite is consistent with solidification of immiscible Fe-Ni metal
293 and silicate melts. Silicate inclusions include inverted pigeonite, feldspar-tridymite lamellae and
294 feldspar-tridymite micrographic textures (Fig. 2; Ikeda et al., 1997, this study), suggesting
295 crystallization from a melt. The silicate inclusions have globular, cuspate and lobate shapes (Fig. 1)
296 demonstrating that the surrounding metal was at least partially molten as they crystallized from a
297 silicate melt.

298 For Miles, our data provide peak temperatures of ~1170°C from two-pyroxene equilibration
299 estimates (following Eqn. 36 in Putirka, 2008) and the presence of disordered srilankite which forms
300 by rapid cooling from ≥1160°C (Troitzsch and Ellis, 2005). The stability limits of tridymite constrains
301 the crystallization to 870-1470 °C (at 0 Pa; Swamy et al., 1994) and pressures less than 0.7 GPa.
302 Consistent with these estimates is the occurrence of ferropseudobrookite in equilibrium with
303 metallic iron at ≥1068 °C (Simons and Woermann, 1978). Two-feldspar equilibration temperatures
304 are ~590°C (following Eqn. 27b in Putirka, 2008) which likely records feldspar reequilibration at
305 subsolidus conditions. In summary, the maximum temperatures for the felsic silicate-bearing Miles
306 are higher than those proposed for IIE iron meteorites with chondritic inclusions such as Netschaëvo
307 (920°C; Van Roosbroek et al., 2015).

308 Oxygen fugacity was calculated previously for the Miles meteorite as IW -1.65 to -1.83 (Ikeda and
309 Prinz, 1996). We find supporting evidence for this with ferropseudobrookite, rutile and metallic iron
310 existing as small grains (<100 μm) within enstatite in inclusion i37. The fO_2 for this phase assemblage
311 in the Fe-Ti-O system at the appropriate temperatures of 1130-1300°C is 12.84 to 14.26 $-\log fO_2$
312 (Simons and Woermann, 1978), placing it 1.43 to 2.09 log units below the iron-wüstite buffer (IW -
313 1.4 to IW -2.09). These oxygen fugacity estimates are also consistent with the absence of zircon
314 ($ZrSiO_4$) and presence of baddeleyite and silica, which form below the IW buffer (Chesters, 1973).

Our observation of silicophosphates in Miles is also consistent with highly reducing conditions because these minerals are found in residual silicate material from the smelting of iron, where iron oxide is reduced to metallic iron under highly reducing conditions (e.g., Warchulski and Szopa, 2014).

4.2 Petrogenesis of silicate inclusions in Miles

Thermodynamic modeling using the FactSage program (Bale et al., 2016) was conducted to assess whether or not the inclusions formed through crystallization of a melt (similar to Wasson, 2017) or if they are instead unequilibrated xenoliths incorporated into the metal (e.g. Netschaëvo; Van Roosbroek et al., 2016). Textural evidence shows that the silicates and most if not all of the metal were initially molten, therefore the system was modelled as cooling from above the metal liquidus. Scheil-Gulliver and equilibrium cooling were both modelled based on the bulk silicate composition estimate for Miles (Table 3). In Scheil-Gulliver cooling the liquid phases remain in equilibrium with each other and the surfaces of the solid phases and peritectic reactions were ignored, similar to Rayleigh (fractional crystallization). In equilibrium cooling, the Gibbs free energy is minimized assuming the bulk composition remains the same at each temperature.

In both models, silicate and oxide phases crystallize predominantly between ~870 and 1220°C, consistent with the temperatures calculated using mineral stability and geothermometry (Fig. 4, Tables S4 and S5). In the Scheil-Gulliver cooling model, ~97% of the metal crystallizes before the silicates (initially augite) begin precipitating at ~1220°C, and in the equilibrium cooling model all of the metal crystallizes by ~1410°C, prior to silicate precipitation.

Figure 4 near here

For both crystallization models there is <1 wt.% difference between the observed and modelled phases at the end of cooling (Table 5). Although K-feldspar is not predicted by either model, the modal percent of K-feldspar is ~0.1 wt.% in Miles, well within the 1% relative values predicted. Compared to the mineral compositions observed in Miles, the predicted mineral compositions are

within 1-3% relative for the equilibrium cooling model and within 7-17% for the Scheil-Gulliver model.

Table 5 near here

Because initial cooling rates in Miles were rapid (Section 4.1), it is more likely that Scheil-Gulliver cooling conditions prevailed. Furthermore, the cuspate margins of silicate inclusions in contact with metal suggest that some metal and silicates crystallized simultaneously as modelled in Scheil-Gulliver cooling but not in equilibrium cooling (Fig. 4B,C). It is possible that subsolidus reequilibration modified the phase compositions bringing them closer to those predicted by the equilibrium model. The close agreement between both thermodynamic models and the observed mineralogy and chemistry of the inclusions is consistent with the formation of the silicate inclusions from a melt. The thermodynamic model suggests that the system cooled from very high temperatures; specifically a modelled silicate liquidus temperature of ≥1220°C (Fig. 4B), in line with geothermometry estimates.

To understand how the diverse compositions of silicate inclusions in the Miles meteorite are achieved (i.e. Type A, B and C), we compared the H chondrite normalized compositions of the inclusions (Table 3), against silicate glasses synthesized by partially melting a H chondrite bulk composition (Fig. 5; Collinet and Grove, 2020). H chondrites were chosen due to their high iron content and proposed relationship to IIE iron meteorites (e.g., McDermott et al., 2016). At the lowest temperatures and melt fractions the synthetic partial melts show the greatest departures from their H chondrite starting composition with higher Si, Al, Na and K (felsic elements) and lower in Fe, and Mg (mafic elements) (Fig. 5). Similar trends are present in the Miles silicate inclusion compositions. Type A inclusions are most similar to the highest degree partial melts (F = 28.3%, synthesized at 1301°C). The compositions of Type B inclusions are consistent with temperatures and melt fraction slightly lower than those of the Type A inclusions. Type C inclusions are most consistent with a low degree partial melt (F= 5%, synthesized at 1085°C) because they show the highest felsic elements, lowest Fe and undetected Mg abundances relative to H chondrites. Type C

364 inclusions contain minerals high in incompatible elements such as Zr, U and Th (Tables 1 and 2). We
365 hypothesize that the chondritic inclusions in many IIE irons formed at low temperatures but do not
366 reflect partial melts but instead xenoliths of the original H chondrite parent body that have been
367 entrained within the metal.

368 *Figure 5 near here*

369 Our major element and geothermometry results agree with the findings of Hsu (2003) who used REE
370 patterns to suggest that the silicate inclusions in Miles formed at different localized temperatures
371 prior to isolation of the melt. In contrast, Ruzicka and Hutson (2010) estimate ~30% partial melting
372 of a chondritic precursor, with equilibration between cumulus minerals and intercumulus melt
373 followed by fractional crystallization to form the observed REE pattern. Buoyancy constraints require
374 that the metal and silicate melts were not in isostatic equilibrium when molten, which implies these
375 isolated silicate inclusions were trapped quickly (within minutes) in the dense liquid metal (e.g.
376 Tomkins et al., 2013). The average 5 mm radius of silicate inclusions in Miles would have floated in
377 the liquid metal at a rate of approximately 0.3 cm/sec on a 1 km body to 90 cm/sec on a 500 km
378 body (see the Supplement for full calculations). This would occur in any melt volume at the surface
379 of the parent body. Because the physical separation of metal and silicate melts is highly efficient and
380 rapid, it is unlikely to occur in a core or large body of metal with a large thermal mass. If instead
381 these meteorites formed in small volumes of melt with a transient heat source and small thermal
382 mass there is a physical mechanism for arresting the separation of the metal and silicate liquid
383 phases.

384 As a mechanism for the formation of silicate inclusions with a range of compositions, we hypothesize
385 that partial melting of parent body material forms silicate melts (Fig. 6A) that ascend between the
386 crystallizing Fe-Ni metal (Fig. 6B). The metal phase was the first to begin crystallizing (Fig. 4B), and
387 once most of the metal was solid buoyancy separation of the silicate and metal phases ceased.
388 Where rapid initial cooling and metal crystallization occurred, the droplets of silicate melt became

trapped along the Fe-Ni parent γ-crystal grain boundaries and junctions (Fig. 6B). The isolated droplets of partial melt continue to cool and crystallize, forming the series of silicate inclusions along Fe-Ni parent metal γ-crystal grain boundaries (Fig. 6C) as seen in the Miles meteorite (Fig. 1B,C). We propose that rapid melting followed by initially rapid cooling to below the Fe-Ni solidus would arrest the buoyancy separation of these phases in this manner. Ruzicka et al. (2006) proposed a similar buoyancy model for Sombrerete, whereby crystal-liquid fractionation of the silicate melt results in the upwards flow of residual silicate melt through the metallic host with already formed silicate crystals being left behind. The thermodynamic modelling for Miles does not support the Ruzicka et al. (2006) model because ≥97% of the metal is modelled to have precipitated prior the crystallization of any silicates, leaving little to no capacity for the migration of evolved melts through the metal host. Our model instead proposes that the inclusions formed from individual, chemically diverse droplets of partial melts that were isolated soon after melting, preserving a diversity of inclusion compositions. We posit that the highly felsic Type C inclusions (Fig. 2) are low fractions of partial melts of the parent body (Fig. 5), not the product of evolved melts from fractional crystallization.

Figure 6 near here

4.3 Formation of schreibersite in the Miles meteorite

Under the high temperature (≥1170°C), low pressure (<0.7 GPa) and low fO_2 (IW -1.43 to -2.09) conditions present at the time of formation, reduction of FeO to metallic iron in the presence of phosphorus and CaO may form calcium phosphates (Muan and Osborn, 1965, Ikeda et al., 1997). This process is described by

$$2Fe_3P + 5FeO + 3CaO \leftrightarrow 11Fe + Ca_3(PO_4)_2 \qquad (1)$$

Oxidation of P in a metallic melt has been inferred for a number of other meteorites, for example IIIAB iron meteorites (Olsen et al., 1999) and the lodranite Graves Nunataks 95209 (McCoy et al., 2006). This reaction is consistent with the petrography of the inclusions where the phosphates commonly form at the margins of silicate inclusions in contact with Fe-Ni metal. We note that this

reaction does not require O_2 (cf. Ruzicka et al., 2005) because oxidation-reduction is achieved through electron transfer between the Fe and P.

This reaction removes P from the metal liquid (Eq. 1), which ultimately results in the formation of a Ca-phosphate-rich silicate melt. Augite is the first silicate phase predicted to precipitate (Fig. 4B,C), removing CaO from the silicate melt and driving a relative increase in SiO_2, Al_2O_3 and Na_2O. This increases the activity of P_2O_5 in the melt, in turn promoting P reversion into the metal through the reversal of Equation 1 (Bodsworth, 1963; Sharp, 1966). Therefore, when augite begins to crystallize, dephosphorization of the metal ceases and reversion of phosphorus begins forming schreibersite where silicate melt is in contact with metal. After further crystallization of the remaining phases in the silicate inclusions, the balance between products and reactants in Equation 1 is reached and calcium phosphates form. Thus, phosphates and phosphides crystallize at the margins of inclusions and metal grain boundaries where silicate and metal melts are in or have been in contact.

4.4 Age of the Miles meteorite

The zirconium and phosphate minerals yield a $^{207}Pb/^{206}Pb$ age for the Miles meteorite of 4542.3 ± 4.0 Ma. This age is similar to that of the chondritic silicate inclusions in Techado and the felsic silicate inclusions in Weekeroo Station and Colomera (Fig. 7). However, our age is considerably older than those previously reported for Miles: ^{40}Ar-^{39}Ar age of 4408 ± 9 Ma (Bogard et al., 2000) and ^{147}Sm-^{143}Nd model age of 4270 Ma – (no error given; Snyder et al., 2001) (Fig. 7).

Figure 7 near here

Two partial plateaus are present in the ^{40}Ar-^{39}Ar spectrum from this study, a high-T partial plateau at 4303 ± 6.9 Ma (18% gas release) and a low-T partial plateau at 3496 ± 52 Ma (22% release) (Fig. 3A). Although gas release for each segment is small (Fig. 3A), the Ca/K is low (Fig. 3B), and the ages of each segment are in agreement with dates obtained for other IIE iron meteorites (Fig. 7). These values are similar to silicate inclusions from four IIE iron meteorites which have K-Ar or ^{40}Ar-^{39}Ar ages of around 4.3-4.5 Ga and four others around 3.4-3.8 Ga (Fig. 7; Bogard et al., 1969; Niemeyer, 1980;

Olsen et al., 1994; Casanova et al., 1995; Bogard et al., 2000). The older ^{40}Ar-^{39}Ar is approximately 240 Myr younger than the $^{207}Pb/^{206}Pb$ we obtained. The discrepancy between the ^{40}Ar-^{39}Ar and $^{207}Pb/^{206}Pb$ obtained may be due to slow cooling through the different closure temperatures of each radioisotopic systems, or it may be due to a later impact event that provided sufficient heat to reset the ^{40}Ar-^{39}Ar system but not the $^{207}Pb/^{206}Pb$ system. Hf-W dating suggests that a series of previous thermal events occurred on the IIE parent body in the first 27 Myr after CAI formation (Kruijer and Kleine, 2019) consistent with our results that show a high-T thermal event occurred at 4542 ± 4 Ma, ~25 Myr after CAI formation. Our study is the first to date silicates in IIE iron meteorites to both 4.542 Ga and 3.5 Ga. We interpret these ages as thermal events related to formation at ~4.54 Ga followed by an impact at 3.5 Ga. The timing of these thermal events may have implications on our understanding of the impact history of the inner solar system (c.f. Bottke and Norman, 2017).

4.5 Petrogenesis of the IIE iron meteorites

Our study of the Miles meteorite indicates a particular thermal history: high peak temperatures (≥1170°C) followed by rapid cooling. However other IIE irons such as Netschaëvo record lower peak temperatures (~920; Van Roosbroek et al., 2015) and slow cooling rates (~3°C/Ma; Rubin, 1990). The IIE group petrogenesis must also account for formation of immiscible metal and silicate melts (Ruzicka and Hutson, 2010), metal that has not fractionated siderophile elements (Wasson, 2017), and inclusions that range in composition from chondritic (Bild and Wasson, 1977) to felsic (Type B-C inclusions; this study). With these petrographical and geochemical features in mind, we examine the various hypotheses of formation to determine the most parsimonious petrogenetic model for the formation of the IIE group of iron meteorites.

Planetary differentiation models (e.g., Wasserburg et al., 1968; McCoy, 1995) have difficulty explaining the co-existance of metal and silicates considering their large buoyancy contrasts (Section 4.2 and e.g. Ruzicka, 2014). To explain the occurrence of differentiated silicates with metal, previous studies have called upon impact mixing of already differentiated components (e.g., Ruzicka and

Hutson, 2010; Ruzicka, 2014; McDermott et al., 2016); however the siderophile element compositions of the metal are inconsistent with a previously differentiated and fractionated metal source (Wasson, 2017). Another explanation given for the presence of felsic silicate glasses in metal is subsolidus metasomatism and condensation (Kurat et al., 2007), but this model does not account for the evidence of immiscible metal and silicate melts. Here we propose a new model for IIE irons that invokes impact-induced partial melting, formation of immsicible metal and silicate melts and trapping of silicate melts produced by variable degrees of melting entrained within a rapidly cooling metallic melt.

Figure 8 near here

IIE iron meteorites with felsic silicate inclusions likely formed from partial melts and we infer that these were derived from high temperatures (e.g., Miles, Weekeroo Station, Kodaikanal, Colomera and Tarahumara). We propose that IIE irons with felsic inclusions formed in melt lenses near the surface of the impact crater (Fig. 8A,E,J) with high porosity in the regolith, higher energy due to proximity to the impact, and rapid cooling. Rapid gravity separation would concentrate metallic melt at the base of the melt lenses and heat diffusion may result in partial melting of the surrounding chondritic rock, forming partial melt droplets up to 30 mm diameter (Fig. 6A). Due to the large density differences between metal and silicate melts, the size that these silicate partial melt droplets could grow to would be limited to the point at which buoyancy forces became great enough to overcome the adhesive forces involved in the wetting of the silicate melt to the mostly silicate solid. These melt droplets would detach from the source material and begin rising through the metal melt (Fig. 6B). Buoyant forcing would cease upon cooling of the crystallizing metal, trapping the silicate melt droplets (Section 4.2, Fig. 6C). A similar process of impact-initiated partial melting in an endogenically heated parent body followed by rapid cooling at the surface has been suggested for Sombrerete (IAB-sHL iron meteorite) by Ruzicka et al. (2006).

We propose that the silicate-free IIE iron meteorites formed through slower cooling, allowing for gravity separation of silicates and the development of Widmanstätten pattern in the metal (e.g., Arlington, Fig. 8F,K). We hypothesize that this occurred in the center of large melt lenses and dikes buried at depth in the regolith (Fig. 8A). If the parent body was already warm through endogenic heating prior to the impact (e.g. Ruzicka and Hutson, 2010; Ruzicka 2014; Kruijer and Kleine, 2019), then the cooling rate will be slower for melts in dikes at depth compared to surface or near-surface melts. This would explain the variety of cooling rates calculated for the IIE iron meteorite group: the warm regolith would insulate melts formed at depth resulting in slow cooling rates whereas those exposed near the surface of the parent body would cool rapidly.

In our proposed model, IIE iron meteorites with chondritic inclusions such as Watson 001, Techado and Mont Dieu formed at the margins of dikes (Fig. 8A,D, I). Here, clasts of chondritic parent body material became entrained within the partially crystalline metal, forming relatively unmodified to thermally metamorphosed xenoliths with a chondritic composition e.g., Techado (Fig. 8I). We suggest that some of the xenoliths subjected to higher temperatures melted and recrystallized, forming inclusions with chondritic compositions but igneous textures such as Watson 001 (Bogard et al., 2000).

We propose that impact forces brecciated the basement rock, with molten metal from overlying melts percolating down through fractures and surrounding the angular clasts forming metal veins (Fig. 8A,C, H). The smaller volumes of metallic melts (compared to lenses and dikes) were unable to heat the surrounding parent body material to the same degree, thereby preserving angular clasts with a chondritic composition and relict chondrules. At these depths in the regolith cooling rates would also be slower. Netschaëvo shows these features, and is analogous of the type of breccia that we expect at the base of the impact crater that formed the IIE iron meteorites (Fig. 8H; Van Roosbroek et al., 2016).

512 Assuming all of the IIE iron meteorites formed in a single impact, then the crater would be a
513 minimum of ~100 m diameter. This was determined using the calculator by Holsapple (2020) with
514 the assumption that the volume of the melt is equal to the volume of the impactor (Davison et al.,
515 2010), and that the entirety of the melt produced is represented by IIE iron meteorites identified in
516 the Meteoritical Bulletin Database (Lunar and Planetary Science Institute, 2020). It is however
517 unlikely that all melt products from the impact have been recovered as meteorites on the Earth. If
518 instead it is assumed that they represent 1% of the melt products, then the crater would be at least
519 ~350 m in diameter. We suggest a maximum crater diameter of 200 km diameter assuming that the
520 parent body had a size similar to the current size distribution of main belt asteroids (≤500 km
521 diameter) and a maximum crater diameter/parent body radius = 0.8 (Burchell and Leliwa-
522 Kopystynski, 2010). It is possible for impact melting in discrete lenses to occur in a range of crater
523 morphologies because these physical processes likely occur under a range of impact conditions
524 (projectile size, velocity, impact angle etc.).

525 Our geochronology results concur with previous workers (e.g., Li et al., 2001, Fig. 7) that most of the
526 IIE irons formed ~25 Ma after the formation of the solar system (4.542 Ga). At this time, heat
527 production through radioactive decay of ^{26}Al alone was not sufficient to cause significant melting
528 (Sahijpal et al., 2007). and kinetic energy from accretion is generally inadequate to melt asteroid-
529 sized solid bodies (Keil et al., 1997). An alternate heating mechanism involves impact into a porous
530 target because the compression and subsequent release of pore spaces results in high temperatures
531 (Kieffer et al., 1976). Porosity in early solar system bodies is likely within clasts (e.g. ordinary
532 chondrites; Bland et al., 2014) and between clasts (e.g. asteroid 162173 Ryugu; Grott et al., 2020). If
533 the numerous thermal events recorded in the Hf-W dates were impacts (Kruijer and Kleine, 2019), it
534 is possible that they formed a fractured and battered regolith. Localized temperatures of up to~
535 2750°C are calculated to occur in a porous ordinary chondrite matrix following a simulated impact at
536 3.00 km s^{-1} (Bland et al., 2014), exceeding temperatures required to form metal and silicate melts on
537 a chondritic body.

We propose that at 4542 ± 4 Ma, the IIE parent body was impacted, with peak temperatures experienced near areas of higher porosity and higher energy (i.e., closer to the impact site) experiencing higher temperatures (Davison et al., 2010; Bland et al., 2014). We posit that this uneven distribution of heating resulted in discrete areas of melting at the impact site forming melt lenses (Fig. 8A). A metallic iron-rich chondritic parent body, similar to H chondrites, would form immiscible silicate and metal melts when subjected to high temperatures. We suggest that these melts would undergo rapid gravity separation upon formation, with the metallic melts flowing down through fractures formed in the base of the crater during the impact, resulting in a series of dikes (Fig. 8A). Because the physical separation of metal and silicate melts is highly efficient and rapid, this process is unlikely to occur in a core or large body of metal with large thermal mass. If instead these meteorites formed in smaller melt lenses and dikes with a transient heat source and small thermal mass there is a physical mechanism for arresting the separation of these phases. We hypothesize that melts formed in the impact immediately began to cool as heat escaped from the body, with the cooling rate depending on the depth of burial within the regolith. This hypothesis is supported by the observations of large melt veins in some chondritic meteorites (e.g., Chico; Bogard et al., 1995) and melt sheets in more coherent larger planetary bodies with higher gravity.

We propose that the younger Ar-Ar, Pb-Pb, K-Ar and Rb-Sr ages of some IIE iron meteorites result from smaller impacts later at ~3.8-3.5 Ga. In this case, widespread melting did not occur. The lower porosity of the solidified metal + silicate melt products, a potentially a smaller impact (with lower impact velocities/smaller impactor/smaller impact angle), and a greater distance to the impact site could have resulted in lower peak temperatures. This explains the age discrepancy between the IIE iron meteorites; Kodaikanal, Netschaëvo and Watson 001 may have been closer to a secondary impact site resetting the K-Ar chronometer, whereas Techado, Weekeroo Station, Colomera and Tarahumara may have been more distal and therefore heated to a lesser extent preserving the older isotopic dates. The gap in impact ages between 4.5 and 3.5-3.7 Ga may have implications for the

temporal distribution of impact events in the asteroid belt (Bottke and Norman, 2017), or it may represent a prolonged period of impact bombardment.

5. Conclusions

Using a combination of geochemical, petrologic and mineralogic studies, and physical and thermodynamic modelling we suggest the IIE iron meteorites have a common history: (1) formation of an H chondrite-like parent body that was battered by multiple impact events creating a porosity and perhaps retaining heat; (2) at 4542 Ma the parent body was impacted by a smaller body creating a significant thermal event, (3) higher porosity regions experienced higher peak temperatures, resulting in partial melting under low oxygen fugacity conditions (IW -1.43 to IW -2.09), (4) immiscible metallic iron and silicate liquids underwent density separation that segregated metallic iron, (5) heat transferred into the surrounding chondritic material resulting in partial melting, forming felsic melts enriched in incompatible elements, (6) rapid cooling of the metallic melts trapped some of these felsic silicates as inclusions in the metal before full separation could occur, with cooling rates slowing as silicates crystallized, (7) metallic melt percolated through fractures in the parent rock beneath melt lenses and dikes, forming metallic veins in thermally metamorphosed chondritic material and entraining chondritic clasts, (8) the body was impacted again between ~ 4300 and 3500 Ma and reheated without significant melting, followed by slow cooling.

We propose the IIE irons experienced peak temperatures and cooling rates that depended on their proximity to the impact site, parent body porosity, and capacity to transfer heat away during cooling. These meteorites sample lenses, dikes and parent body material in and around the impact structure in which each experienced a different temperature and cooling history, resulting in a wide variety of chemical and mineralogical features amongst the group. Impact events such as the one that formed the IIE iron meteorites were common in the early solar system so impact melting is anticipated to have occurred on other bodies. On less iron-rich bodies, such as Vesta, similar

processes are expected to have occurred but the resulting meteorites are unlikely to have large volumes of metallic iron.

Acknowledgements

Many thanks to Richard Arculus and David Gust for providing the sample of the Miles meteorite. Richard Henley is thanked for advice and guidance on an earlier version of the manuscript. Funding for the project came from the Australian Research Council DP150104604, DP200100406 and FT130101524 (King), the Australian Synchrotron IA161/10908, and the Advanced Light Source ALS-07585 (Troitzsch & King). This research used beamline 12.3.2 of the Advanced Light Source, which is a DOE Office of Science User Facility under contract no. DE-AC02-05CH11231. We gratefully acknowledge support by an AGRTPSS granted by the Australian Government Research Training Program and an RSES John Conrad Jaeger Scholarship (Kirby). The authors acknowledge the facilities, and the scientific and technical assistance, of Frank Brink and the Australian Microscopy & Microanalysis Research Facility at the Centre of Advanced Microscopy, The Australian National University.

References

Armstrong J. T., Kennedy A. K., Carpenter P. K. and Albee A. L. (1990) Petrography and trace element chemistry of Colomera (IIE) silicate inclusions: rhyolitic plums in the pudding. *Lunar Planet. Sci. Conf.* **21**, 22–23.

Bale C. W., Bélisle E., Chartrand P., Decterov S. A., Eriksson G., Gheribi A. E., Hack K., Jung I. H., Kang Y. B., Melançon J., Pelton A. D., Petersen S., Robelin C., Sangster J., Spencer P. and Van Ende M. A. (2016) Reprint of: FactSage thermochemical software and databases, 2010–2016. *Calphad Comput. Coupling Phase Diagrams Thermochem.* **55**, 1–19.

Bild R. W. and Wasson J. T. (1977) Netschaevo: A New Class of Chondritic Meteorite. *Science (58-61).* **197**, 58–62.

Birck J. L. and Allègre C. J. (1998) Rhenium-187-osmium-187 in iron meteorites and the strange origin

of the Kodaïkanal meteorite. *Meteorit. Planet. Sci.* **33**, 647–653.

Bland P. A., Collins G. S., Davison T. M., Abreu N. M., Ciesla F. J., Muxworthy A. R. and Moore J. (2014) Pressure-temperature evolution of primordial solar system solids during impact-induced compaction. *Nat. Commun.* **5**, 1–13.

Bodsworth C. (1963) *Physical Chemistry of Iron and Steel Manufacture*., Longmans, Green and Co Ltd, London.

Bogard D. D., Burnett D. S., Eberhardt P. and Wasserburg G. J. (1967) ^{40}Ar - ^{40}K ages of silicate inclusions in iron meteorites. *Earth Planet. Sci. Lett.* **3**, 275–283.

Bogard D. D., Burnett D. S. and Wasserburg G. J. (1969) Cosmogenic rare gases and the ^{40}K-^{40}Ar age of the Kodaikanal iron meteorite. *Earth Planet. Sci. Lett.* **5**, 273–281.

Bogard D. D., Garrison D. H. and McCoy T. J. (2000) Chronology and petrology of silicates from IIE iron meteorites: Evidence of a complex parent body evolution. *Geochim. Cosmochim. Acta* **64**, 2133–2154.

Bogard D. D., Garrison D. H., Norman M., Scott E. R. D. and Keil K. (1995) ^{39}Ar-^{40}Ar age and petrology of Chico: Large-scale impact melting on the L chondrite parent body. *Geochim. Cosmochim. Acta* **59**, 1383–1399.

Bottke W. F. and Norman M. D. (2017) The Late Heavy Bombardment. *Annu. Rev. Earth Planet. Sci.* **45**, 619–647.

Buchwald V. F. (1975) *Handbook of Iron Meteorites*., University of California Press, Berkeley.

Bunch T. E., Keil K. and Olsen E. (1970) Mineralogy and petrology of silicate inclusions in iron meteorites. *Contrib. to Mineral. Petrol.* **25**, 297–340.

Burchell M.J. and Leliwa-Kopystynski J. (2010) The large crater on the small Asteroid (2867) Steins. *Icarus* **210**, 707-712.

635 Burnett D. S. and Wasserburg G. J. (1967a) ^{87}Rb-^{87}Sr ages of silicate inclusions in iron meteorites.
636 *Earth Planet. Sci. Lett.* **2**, 397–408.

637 Burnett D. S. and Wasserburg G. J. (1967b) Evidence for the formation of an iron meteorite at 3.8 x
638 10^9 years. *Earth Planet. Sci. Lett.* **2**, 137–147.

639 Casanova I., Graf T. and Marti K. (1995) Discovery of an unmelted H-chondrite inclusion in an iron
640 meteorite. *Science* **268**, 540–542.

641 Chabot N. L. and Haack H. (2006) Evolution of Asteroidal Cores. In *Meteorites and the Early Solar*
642 *System II* (eds. D. S. Lauretta and H. Y. McSween Jr.). University of Arizona Press, Tucson. pp.
643 747–771.

644 Chesters J. H. (1973) *Refractories: Production and Properties*., The Iron and Steel Institute, London.

645 Collinet M. and Grove T. L. (2020) Widespread production of silica- and alkali-rich melts at the onset
646 of planetesimal melting. *Geochim. Cosmochim. Acta* **277**, 334–357.

647 Connelly J. N., Bizzarro M., Krot A. N., Nordlund Å., Wielandt D. and Ivanova M. A. (2012) The
648 Absolute chronology and thermal processing of solids in the solar protoplanetary disk. *Science*
649 **338**, 651–655.

650 Davison T. M., Collins G. S. and Ciesla F. J. (2010) Numerical modelling of heating in porous
651 planetesimal collisions. *Icarus* **208**, 468–481.

652 Evensen N. M., Hamilton P. J., Harlow G. E., Klimentidis R., O'Nions R. K. and Prinz M. (1979) Silicate
653 inclusions in Weekeroo Station: Planetary differentiates in an iron meteorite. *Lunar Planet. Sci.*
654 **10**, 376–378.

655 Forster M. A. and Lister G. S. (2004) The interpretation of ^{40}Ar/^{39}Ar apparent age spectra produced
656 by mixing: Application of the method of asymptotes and limits. *J. Struct. Geol.* **26**, 287–305.

657 Forster M. and Lister G. (2009) Core-complex-related extension of the Aegean Lithosphere initiated

at the Eocene-Oligocene transition. *J. Geophys. Res. Solid Earth* **114**, 1–36.

Goldstein J. I., Scott E. R. D. and Chabot N. L. (2009) Iron meteorites: Crystallization, thermal history, parent bodies, and origin. *Chemie der Erde* **69**, 293–325.

Göpel C., Manhes G. and Allègre C. J. (1985) Concordant 3676 Myr U-Pb formation age for the Kodaikanal iron meteorite. *Nature* **317**, 341–344.

Grott M., Biele J., Michel P., Sugita S., Schröder S. E., Sakatani N., Neumann W., Kameda S., Michikami T. and Honda C. (2020) Macroporosity and grain density of rubble pile asteroid (162173) Ryugu. *J. Geophys. Res. Planets* **125**, 1–15.

Holsapple K. A. (2020) Impact and Explosion Effects. *Univ. Washington.* Available at: http://keith.aa.washington.edu/craterdata/scaling/index.htm [Accessed July 22, 2020].

Hsu W. (2003) Rare earth element geochemistry and petrogenesis of Miles (IIE) silicate inclusions. *Geochim. Cosmochim. Acta* **67**, 4807–4821.

Ikeda Y., Ebihara M. and Prinz M. (1997) Petrology and chemistry of the Miles IIE iron. I: Description and petrology of twenty new silicate inclusions. *Antarctic Meteor. Res.* **10**, 355–372.

Ikeda Y. and Prinz M. (1996) Petrology of silicate inclusions in the Miles IIE iron. In *Proc. NIPR Symp. Antarct. Meteorites* **9**, 143-173.

Ireland T. R., Clement S., Compston W., Foster J. J., Holden P., Jenkins B., Lanc P., Schram N. and Williams I. S. (2008) Development of SHRIMP. *Aust. J. Earth Sci.* **55**, 937–954.

Ireland T. R. and Williams I. S. (2003) Considerations in zircon geochronology by SIMS. *Rev. Mineral. Geochemistry* **53**, 215–241.

Jarosewich E. (1990) Chemical analyses of meteorites: A compilation of stony and iron meteorite analyses. *Meteoritics* **25**, 323–337.

Keil K., Stoffler D., Love S. G. and Scott E. R. D. (1997) Constraints on the role of impact heating and

melting in asteroids. *Meteorit. Planet. Sci.* **32**, 349–363.

Kieffer S. W., Phakey P. P. and Christie J. M. (1976) Shock processes in porous quartzite: Transmission electron microscope observations and theory. *Contrib. to Mineral. Petrol.* **59**, 41–93.

Kruijer T. S. and Kleine T. (2019) Age and origin of IIE iron meteorites inferred from Hf-W chronology. *Geochim. Cosmochim. Acta* **262**, 92–103.

Kurat G., Zinner E. and Varela M. E. (2007) Trace element studies of silicate-rich inclusions in the Guin (UNGR) and Kodaikanal (IIE) iron meteorites. *Meteorit. Planet. Sci.* **42**, 1441-1463.

Li S., Nemchin A., Che X., Liu D., Long T., Luo Y., Beard S. and Tang C. (2021) Multiple thermal events recorded in IIE silicate inclusions : Evidence from in situ U-Pb dating of phosphates in Weekeroo Station. *Geochim. Cosmochim. Acta* **309**, 79–95.

Limaye A. (2012) Drishti: a volume exploration and presentation tool. In *Proc. SPIE 8506, Developments in X-Ray Tomography VIII* p. 85060X.

Lodders K. (2003) Solar system abundances and condensation temperatures of the elements. *Astrophys. J.* **591**, 1220-1247.

Lunar and Planetary Science Institute (2020) Meteoritical Bulletin Database. *Meteorit. Soc.* Available at: https://www.lpi.usra.edu/meteor/metbull.php? [Accessed July 22, 2020].

Markowski A., Quitté G., Halliday A.N. and Kleine T. (2006) Tungsten isotopic compositions of iron meteorites: Chronological constraints vs. cosmogenic effects. *Earth Planet. Sci. Lett.* **242**, 1-15.

McCoy T. J. (1995) Silicate-bearing IIE irons: early mixing and differentiation in a core-mantle environment and shock resetting of ages. *Meteoritics* **30**, 542–543.

McCoy T. J., Carlson W. D., Nittler L. R., Stroud R. M., Bogard D. D. and Garrison D. H. (2006) Graves Nunataks 95209: A snapshot of metal segregation and core formation. *Geochim. Cosmochim.*

704 *Acta* **70**, 516–531.

705 McDermott K. H., Greenwood R. C., Scott E. R. D., Franchi I. A. and Anand M. (2016) Oxygen isotope
706 and petrological study of silicate inclusions in IIE iron meteorites and their relationship with H
707 chondrites. *Geochim. Cosmochim. Acta* **173**, 97–113.

708 Muan A. and Osborn E. F. (1965) *Phase Equilibria Among Oxides in Steelmaking*., Addison-Wesley
709 Pub. Co.

710 Niemeyer S. (1980) I-Xe and ^{40}Ar-^{39}Ar dating of silicate from Weekeroo Station and Netschaëvo IIE
711 iron meteorites. *Geochim. Cosmochim. Acta* **44**, 33–44.

712 Olsen E. J., Davis A. M., Clarke R. S., Schultz L., Weber H. W., Clayton R. N., Mayeda T. K., Jarosewich
713 E., Sylvester P., Grossman L., Wang M. S., Lipschutz M. E., Steele I. M. and Schwade J. (1994)
714 Watson: A new link in the IIE iron chain. *Meteoritics* **29**, 200–213.

715 Olsen E. J., Kracher A., Davis A. M., Steele I. M., Hutcheon I. D. and Bunch T. E. (1999) The
716 phosphates of IIIAB iron meteorites. *Meteorit. Planet. Sci.* **34**, 285–300.

717 Olsen E. and Jarosewich E. (1971) Chondrules: First occurrence in an iron meteorite. *Science* **174**,
718 583–585.

719 Putirka K. D. (2008) Thermometers and barometers for volcanic systems. *Rev. Mineral. Geochemistry*
720 **69**, 61–120.

721 Qin L., Dauphas N., Wadhwa M., Masarik J. and Janney P.E. (2008) Rapid accretion and
722 differentiation of iron meteorite parent bodies inferred from ^{182}Hf-^{182}W chronometry and
723 thermal modeling. *Earth Planet. Sci. Lett.* **273**, 94-104.

724 Rubin, A.E., 1990. Kamacite and olivine in ordinary chondrites: intergroup and intragroup
725 relationships. *Geochim. Cosmochim. Acta* **54**, 1217-1232.

726 Ruzicka A. (2014) Silicate-bearing iron meteorites and their implications for the evolution of

asteroidal parent bodies. *Chemie der Erde* **74**, 3–48.

Ruzicka A., Hutson M. and Floss C. (2006) Petrology of silicate inclusions in the Sombrerete ungrouped iron meteorite: Implications for the origins of IIE-type silicate-bearing irons. *Meteorit. Planet. Sci.* **41**, 1797-1831.

Ruzicka A. and Hutson M. (2010) Comparative petrology of silicates in the Udei Station (IAB) and Miles (IIE) iron meteorites: Implications for the origin of silicate-bearing irons. *Geochim. Cosmochim. Acta* **74**, 394–433.

Ruzicka A., Killgore M., Mittlefehldt D. W. and Fries M. D. (2005) Portales valley: Petrology of a metallic-melt meteorite breccia. *Meteorit. Planet. Sci.* **40**, 261-295.

Ruzicka A., Snyder G. A., Prinz M., Papike J. J. and Taylor L. A. (1999) Petrogenesis of silicate inclusions in the Weekeroo Station IIE iron meteorite: Differentiation, remelting, and dynamic mixing. *Geochim. Cosmochim. Acta* **63**, 2123–2143.

Sahijpal S., Soni P. and Gupta G. (2007) Numerical simulations of the differentiation of accreting planetesimals with 26Al and 60Fe as the heat sources. *Meteorit. Planet. Sci.* **42**, 1529–1548.

Sanz H. G., Burnett D. S. and Wasserburg G. J. (1970) A precise $^{87}Rb/^{87}Sr$ age and initial $^{87}Sr/^{86}Sr$ for the Colomera iron meteorite. *Geochim. Cosmochim. Acta* **34**, 1227-1239.

Scherstén A., Elliiott T., Hawkesworth C., Russell S. and Masarik J. (2006) Hf-W evidence for rapid differentiation of iron meteorite parent bodies. *Earth Planet. Sci. Lett.* **241**, 530-542.

Schulz T., Upadhyay D., Münker C. and Mezger K. (2012) Formation and exposure history of non-magmatic iron meteorites and winonaites: Clues from Sm and W isotopes. *Geochim. Cosmochim. Acta* **85**, 200-2012.

Scott E. R. D. and Wasson J. T. (1975) Classification and properties of iron meteorites. *Rev. Geophys.* **13**, 527–546.

750 Scott E. R. D. and Wasson J. T. (1976) Chemical classification of iron meteorites-VIII. Groups IC. IIE,
751 IIIF and 97 other irons. *Geochim. Cosmochim. Acta* **40**, 103–115.

752 Sharp J. D. (1966) *Elements of Steelmaking Practice*., Pergamon Press, Oxford, United Kingdom.

753 Simons B. and Woermann E. (1978) Iron titanium oxides in equilibrium with metallic iron. *Contrib. to*
754 *Mineral. Petrol.* **66**, 81–89.

755 Snyder G. A., Lee D. C., Ruzicka A. M., Prinz M., Taylor L. A. and Halliday A. N. (2001) Hf-W, Sm-Nd,
756 and Rb-Sr isotopic evidence of late impact fractionation and mixing of silicates on iron
757 meteorite parent bodies. *Earth Planet. Sci. Lett.* **186**, 311–324.

758 Spell T. L. and McDougall I. (2003) Characterization and calibration of $^{40}Ar/^{39}Ar$ dating standards.
759 *Chem. Geol.* **198**, 189–211.

760 Steiger R. H. and Jäger E. (1977) Subcommission on Geochronology: Convention on the use of decay
761 constants in geo- and cosmochronology. *Earth Planet. Sci. Lett.* **36**, 359–362.

762 Swamy V., Saxena S.K., Sundman B., Zhang J. (1994) A thermodynamic assessment of silica phase
763 diagram. *J. Geophys. Res. Solid Earth* **99**, 11787-11794.

764 Takeda H., Bogard D. D., Otsuki M. and Ishii T. (2003) Mineralogy and Ar-Ar age of the Tarahumara
765 IIE iron, with reference to the origin of alkali-rich materials. In *National Institute of Polar*
766 *Research Annual Meeting*

767 Tamura N. (2014) XMAS: A versatile tool for analysing synchrotron X-ray microdiffraction data. In
768 *Strain and Dislocation Gradients from Diffraction* (eds. R. Barabash and G. Ice). World Scientific.
769 pp. 125–155.

770 Tamura N., Kunz M., Chen K., Celestre R. S., MacDowell A. A. and Warwick T. (2009) A superbend X-
771 ray microdiffraction beamline at the advanced light source. *Mater. Sci. Eng. A* **524**, 28–32.

772 Tomkins A. G., Mare E. R. and Raveggi M. (2013) Fe-carbide and Fe-sulfide liquid immiscibility in IAB

meteorite, Campo del Cielo: Implications for iron meteorite chemistry and planetesimal core compositions. *Geochim. Cosmochim. Acta* **117**, 80–98.

Troitzsch U. and Ellis D. J. (2005) The ZrO_2-TiO_2 phase diagram. *J. Mater. Sci.* **40**, 4571–4577.

Van Roosbroek N., Debaille V., Pittarello L., Goderis S., Humayun M., Hecht L., Jourdan F., Spicuzza M. J., Vanhaecke F. and Claeys P. (2015) The formation of IIE iron meteorites investigated by the chondrule-bearing Mont Dieu meteorite. *Meteorit. Planet. Sci.* **50**, 1173–1196.

Van Roosbroek N., Pittarello L., Greshake, A., Debaille, V. and Claeys, P. (2016) First finding of impact melt in the IIE Netschaëvo meteorite. *Meteorit. Planet. Sci.* **51**, 372-389.

Warchulski R. and Szopa K. (2014) Phase composition of Katowice – Wełnowiec pytometallurgical slags: preliminary SEM study. *Contemp. Trends Geosci.* **3**, 77–82.

Wasserburg G. J., Sanz H. G. and Bence A. E. (1968) Potassium-feldspar phenocrysts in the surface of colomera, and iron ieteorite. *Science* **161**, 684–687.

Wasson J. T. (2017) Formation of non-magmatic iron-meteorite group IIE. *Geochim. Cosmochim. Acta* **197**, 396–416.

Tables

Table 1: Inclusion type, size, and mineralogy converted to estimated weight % of each mineral exposed using mineral density.

Type A	Size (mm^2)	Ab	Aug	En	Ap	Mrl	Chr
i2	0.49	7.48	92.52	-	-	-	-
i3	0.55	23.86	19.25	36.73	19.85	-	0.30
i4	0.31	1.34	55.54	42.70	-	-	0.42
i6	4.18	39.51	24.35	30.34	0.03	3.99	1.79
i8	5.41	29.47	62.23	8.30	-	-	-
i13	2.45	21.35	54.86	18.92	3.84	1.03	-
i14	1.48	5.29	42.44	49.20	3.18	-	-
i15	-	x	x	x	-	-	x
i17	1.69	28.98	41.49	29.53	-	-	-
i18	5.38	97.40	0.31	2.29	-	-	-
i19	8.56	34.03	59.92	5.12	-	0.92	-
i23	-	x	x	x	-	-	-
i24	-	x	x	x	-	-	-
i25	-	x	x	-	-	-	-
i31	-	x	-	-	x	-	-
i32	-	x	x	x	-	-	-
i33	-	x	x	x	x	x	x
i38	4.32	28.88	69.19	-	1.94	-	-
i40	1.61	0.66	98.80	-	0.54	-	-
i41	6.29	47.00	49.50	3.02	0.05	-	0.43

Type B	Size (mm^2)	Ab	Aug	En	Ap	Mrl	Chr	Kfs	Trd	Rt	FeS	Kar
i1	2.42	88.07	1.39	-	-	-	-	10.54	-	-	-	-
i5	0.14	14.78	49.65	33.85	-	-	-	1.73	-	-	-	-

i7	7.78	15.81	33.84	44.92	4.00	-	1.11	-	0.33	-	-	-
i9	13.13	43.12	42.63	11.77	-	0.13	0.15	0.49	1.63	0.08		-
i10	0.54	6.89	89.71	-	-	-	-	3.40	-	-	-	-
i16	19.87	73.80	19.44	3.68	0.11	-	-	2.97	-	-	-	-
i22	-	x	x	x	x	-	-	x	x	x	x	-
i26	-	x	x	x	x	-	-	-	x	-	-	-
i34	-	x	x	x	-	x	-	x	x	-	x	-
i35	-	x	x	x	-	-	x	x	x	-	-	-
i36	-	x	x	x	-	-	-	x	-	-	-	-
I37	-	x	x	x	x	x	x	x	-	x	x	x
i39	1.15	78.18	4.92	6.34	1.88	-	-	8.69	-	-	-	-

791

Type C	Size (mm^2)	Ab	Mrl	Chr	Kfs	Trd	Rt	FeS	Ilm	Bdy	Srl	Zrc	Th-Zrc	Si-Ph
i11	0.19	20.48	tr.	-	23.28	54.35	1.89	-	tr.	tr.	tr.	tr.	tr.	tr.
i29	-	x	-	x	x	x	x	x	-	-	x	-	-	-

792

Total	Ab	Aug	En	Kfs	Ap	Trd	Mrl	Chr	Rt	Fe-m	Sch
Silicate inclusion	45.83	39.01	12.21	1.14	0.84	0.37	0.33	0.25	0.02	-	
Bulk meteorite ***	3.54	3.01	0.94	0.09	0.06	0.03	0.03	0.02	0.00	89.53	2.74

793

794 Key to inclusion types: Type A = **Ab + (Aug and/or En)**, Type B = **Ab + Aug + (Kfs and/or Trd)** ± En,
795 Type C = **Ab + Kfs + Trd**, Type An = anomalous inclusions that do not fit the other groups. All groups
796 contain varying amounts of phosphates and accessory oxide phases.

797 Key to mineral abbreviations and average compositions: x = detected but not measured, - = not
798 detected, tr. = trace mineral, Ab = albite ($Ab_{93}An_4Or_3$), Aug = augite ($Wo_{41}En_{48}Fs_{11}$), En = enstatite
799 ($Wo_2En_{80}Fs_{18}$**), Kfs = K-feldspar ($Ab_7An_{<1}Or_{92}$) , Trd = tridymite (SiO_2), Fo = forsterite ($Fo_{95}Fa_5$), Ap =
800 chlorapatite ($Ca_5(PO_4)_3Cl$) , Mrl = merrillite ($Ca_9NaMg(PO_4)_6$), Chr = Cr-spinel ($(Fe,Mg)(Al,Cr)_2O_4$), Rt =

rutile(TiO_2), Kar = ferropseudobrookite ($FeTi_2O_5$), Ilm = ilmenite-geikielite ($(Fe,Mg)TiO_3$), Bdy = baddeleyite (ZrO_2), Srl = srilankite ($Ti_{0.64}Zr_{0.36}O_2$), Zrc = zirconolite ($CaZrTi_2O_7$), Th-bearing zirconolite, Si-Ph = Fe-silicophosphate, FeS = troilite, Fe-m = Fe-Ni-metal (kamacite (7 wt.% Ni) and taenite (25-40 wt.% Ni)), Sch = schreibersite ($(Fe,Ni)_3P$).

Assumed mineral densities for estimated major element compositions (in g cm^{-3}) are Aug = 3.278, En = 3.189, Ab = 2.615, Kfs = 2.56, Trd = 2.28, Mrl = 2.88, Ap = 3.172, Chr = 4.414, Rt = 4.26, Fe-Ni metal = 7.9

*Fe-m was only found in the anomalous inclusion i21 therefore it is not considered when determining the total weight % of phases analyzed.

** Enstatite average composition does not include inclusion i21 analyses as they are anomalously high in Mg and low in Fe.

*** Total bulk silicate inclusion composition excludes the anomalous inclusions i21 and is weighted to account for different inclusion sizes. Bulk meteorite is calculated using the total bulk silicate inclusion composition, 20 vol.% silicates and 3.2 vol.% schreibersite in Miles.

Table 2: Average major element composition of mineral phases (wt.% oxide).

wt.% *1σ*	Trd	Ab	Kfs	En	Aug	Fo	Mrl	Ap	Chr	Rt	Srl	Bdy	Zrc	Th-Zrc	Ilm	Kar	SiPh
n	17	53	15	33	27	5	9	10	12	8	7	3	2	2	1	1	4
SiO_2	98.88 *1.40*	67.89 *2.16*	65.18 *0.91*	56.01 *1.13*	54.08 *1.02*	41.10 *0.98*	0.35 *0.56*	1.05 *1.40*	0.30 *0.55*	0.15 *0.42*	0.12 *0.32*	1.34 *1.40*	-	0.53 *0.75*	56.77	4.74	26.14 *1.60*
TiO_2	-	-	-	0.28 *0.20*	0.70 *0.76*	-	-	-	1.14 0.70	98.62 *1.91*	49.86 *1.17*	0.54 *0.93*	39.40 *0.99*	39.00 *1.44*	-	62.45	0.22 *0.43*
Al_2O_3	1.04 *0.46*	19.78 *1.09*	17.95 *0.39*	0.26 *0.53*	0.55 *0.48*	-	-	-	5.48 *2.82*	-	-	-	-	-	-	-	1.26 *0.16*
Cr_2O_3	-	-	-	0.17 *0.24*	1.61 *0.83*	-	-	-	62.74 *3.86*	0.23 *0.66*	-	-	0.57 *0.81*	1.21 *0.08*	29.35	-	-
FeO*	0.12 *0.38*	0.59 *0.87*	0.55 *0.50*	11.83 *2.78*	6.55 *1.01*	5.59 *0.99*	1.16 *1.36*	1.27 *1.52*	23.13 *5.45*	0.40 *0.43*	0.49 *0.65*	-	2.27 *0.13*	2.67 *1.13*	1.77	26.51	35.83 *2.33*
MnO	-	-	-	0.33 *0.39*	-	-	-	-	0.60 *0.55*	-	-	-	-	-	10.07	-	-
MgO	-	-	-	28.93 *5.56*	16.34 *0.83*	53.95 *1.07*	3.54 *0.16*	0.29 *0.62*	5.93 *2.62*	-	-	-	-	0.29 *0.41*	-	0.42	-
CaO	-	0.88 *0.67*	-	2.06 *5.11*	19.25 *1.19*	-	45.28 *1.40*	51.10 *1.42*	-	-	-	-	11.96 *0.49*	10.26 *2.20*	-	0.50	7.53 *1.55*
Na_2O	0.40 *0.36*	10.43 *0.54*	1.18 *0.97*	0.10 *0.21*	0.93 *0.39*	-	2.57 *0.18*	-	-	-	-	-	-	-	-	-	0.22 0.43
K_2O	-	0.55 *0.28*	14.51 *1.77*	-	-	-	-	-	-	-	-	-	-	-	-	-	0.58 *0.38*
P_2O_5	-	-	-	-	-	-	47.60 *1.89*	40.90 *1.40*	-	-	-	-	-	-	-	2.24	12.62 *2.69*
Cl	-	-	-	-	-	-	-	5.45 *0.26*									
ZnO									1.10 *0.98*	-	-	-	-	-	-	-	-
ZrO_2									-	0.20 *0.38*	51.20 *1.32*	98.53 *4.50*	44.03 *1.32*	40.89 *2.70*	-	-	-

ThO_2									-	-	-	-	-	3.22 *2.91*	-	-	-
V_2O_3									-	0.08 *0.23*	-	-	-	-	-	-	-
NiO									-	-	-	-	-	-	-	3.14	1.93 *1.35*
Total	100.44	100.13	99.38	99.96	100.00	100.65	100.49	100.07	100.42	99.60	101.67	100.41	98.24	98.05	97.95	100.00	86.33
Area (%) #	0.37	45.44	1.13	12.23	38.68	0.14	0.73	0.87	0.39	0.02	tr.	tr.	tr.	tr.	tr.	tr.	tr.

816 Note: Total Fe reported as FeO*. Results below limit of detection (0.5 wt.%) denoted with a hyphen. n is number of analyses., italics is 1 S.D. # Total area %

817 of inclusions mapped and analyzed. The low SiPh is likely due to presence of a hydroxyl or carbonate group unable to be detected on the SEM.

818 **Table 3:** Estimated major element chemistry of inclusions and the area weighted average of analyzed silicate inclusions (excluding the anomalous inclusion

819 i21).

	Type A														Type B								Type C		
Inclusion	i2	i3	i4	i6	i8	i13	i14	i17	i18	i19	i38	i40	i41	Ave.	i1	i5	i7	i9	i10	i16	i39	Ave.	i11	Area weighted average*	Ave. H chondrite **
SiO_2	55.11	47.45	54.92	57.04	58.32	54.83	54.14	58.69	67.58	58.39	57.04	53.89	60.37	56.60	67.40	57.01	54.62	60.87	55.41	64.62	64.97	61.41	82.80	60.13	36.60
TiO_2	0.65	0.18	0.42	0.23	0.46	0.41	0.33	0.33	0.06	0.44	0.50	0.69	0.38	0.38	0.07	0.38	0.29	0.42	0.63	0.18	0.09	0.29	1.91	0.33	0.12
Al_2O_3	1.99	4.92	0.69	8.11	6.19	4.57	1.39	6.03	19.27	7.08	6.10	0.68	9.60	5.72	19.31	3.58	3.48	8.91	2.47	15.25	17.06	11.09	8.77	9.52	2.14
Cr_2O_3	1.49	0.53	1.19	1.54	1.01	0.90	0.72	0.70	0.03	0.98	1.12	1.59	1.08	1.01	0.04	0.83	1.28	0.80	1.45	0.33	0.10	0.59	0.01	0.80	0.52
FeO*	6.10	6.06	8.79	5.87	5.23	6.01	8.65	6.38	0.87	4.74	4.72	6.48	3.97	5.84	0.66	7.34	7.92	4.48	5.93	2.16	1.59	3.69	0.28	4.34	10.30
MnO	0.05	0.12	0.16	0.12	0.06	0.09	0.17	0.11	0.01	0.05	0.04	0.06	0.04	0.09	-	0.13	0.16	0.06	0.05	0.02	0.02	0.05	-	0.06	0.31
MgO	15.12	13.83	21.43	12.99	12.57	14.48	21.13	15.31	0.72	11.31	11.31	16.14	8.99	13.85	0.24	17.89	18.58	10.38	14.66	4.25	2.65	8.34	-	9.92	23.26
CaO	17.87	14.89	11.67	7.54	12.43	13.60	10.95	8.91	0.97	12.37	14.56	19.30	10.04	11.77	1.05	10.45	9.71	8.91	17.33	4.53	2.74	7.50	0.18	8.76	1.74

Na_2O	1.64	2.69	0.68	4.47	3.66	2.77	0.97	3.42	10.16	4.13	3.66	0.99	5.36	3.33	9.28	2.04	1.99	4.91	1.58	7.90	8.27	5.66	2.54	5.16	0.86
K_2O	0.04	0.13	0.01	0.22	0.16	0.12	0.03	0.16	0.54	0.19	0.16	0.00	0.26	0.15	2.09	0.34	0.09	0.31	0.56	0.86	1.76	0.99	3.66	0.43	0.09
P_2O_5	-	8.12	-	1.91	-	2.06	1.30	-	-	0.44	0.79	0.22	0.02	1.18	-	-	1.64	0.06	-	0.05	0.77	0.15	-	0.50	0.27
Cl	-	1.08	-	-	-	0.21	0.17	-	-	-	0.11	0.03	-	0.13	-	-	0.22	-	-	0.01	0.10	0.02	-	0.05	n.r.
ZnO	-	-	-	0.02	-	-	-	-	-	-	-	-	-	-	-	-	0.01	-	-	-	-	-	-	0.00	n.r.
V_2O_3	-	-	-	-	-	-	-	-	-	-	-	-	-	-	-	-	-	-	-	-	-	-	0.01	0.00	n.r.
Fe	-	-	-	-	-	-	-	-	-	-	-	-	-	-	-	-	-	-	-	-	-	-	-	-	15.98
Ni	-	-	-	-	-	-	-	-	-	-	-	-	-	-	-	-	-	-	-	-	-	-	-	-	1.74

820 * Area weighted average of all inclusions where exposed mineral area analyses were conducted, excluding the anomalous inclusion i21.

821 ** From Jarosewich, 1990. n.r. = not reported.

822 **Table 4:** In-situ SHRIMP Pb isotope analyses

Inclusion	Mineral	Label	No. Scans	$^{204}Pb/^{206}Pb$	± (1σ)	$^{207}Pb/^{206}Pb$	± (1σ)	U (ppm)	Th (ppm)	Th/U	Age* (Ma)	Error (Ma) (1σ)
i29	Srilankite-1	ZrTi-1.1	4	3.20E-05	4.3E-05	0.61437	1.0075E-03	52.46	70.00	1.33	4541.9	4.3500
i29	Srilankite-1	ZrTi-1.2A	7	1.78E-05	3.0E-05	0.61407	9.4009E-04	82.08	118.18	1.44	4541.4	2.9800
i29	Srilankite-1	ZrTi-1.2B	7	2.58E-05	2E-06	0.6158	1.8247E-03	59.23	89.09	1.50	4545.4	3.9600
i11	Zirconolite-1	Zirk-1	7	5.55E-06	8.8E-05	0.61307	1.2588E-03	23.69	527.27	22.26	4539.2	6.2700
i11	Zirconolite-2	Zirk-2A	7	9.36E-03	1.0664E-02	0.6323	1.6811E-03	0.25	12.73	50.14	4437.2	93.310
i11	Zirconolite-2	Zirk-2B	7	-4.75E-05	2.682E-03	0.62472	2.6546E-03	0.80	18.18	22.86	4567.2	31.070
i11	Baddeleyite-1	Bad-1	7	1.61E-02	0.23368E-02	0.69904	2.2402E-02	0.63	0.49	0.77	4513.1	209.32
i7	Chlorapatite-1	ClAp-2	7	1.77E-02	5.702E-03	0.61653	1.3332E-02	0.24	1.18	4.99	4163.3	581.50
i7	Chlorapatite-1	ClAp-3	7	-2.29E-03	6.71E-04	0.64028	3.3309E-02	0.17	0.85	5.00	4628.8	270.04

823 *Age is determined from the $^{204}Pb/^{206}Pb$-corrected $^{207}Pb/^{206}Pb$ age.

824 **Table 5:** Observed composition of the Miles meteorite compared to the phases calculated to form under both Scheil-Gulliver Cooling and Equilibrium

825 Cooling using the FactSage database

	Observed		Scheil-Gulliver Cooling		Equilibrium Cooling	
Phase	Estimated amount (wt.%)	Ave. molar composition	Amount (wt.%)	Ave. molar composition	Amount (wt.%)	Ave. molar composition
Fe-Ni metal + Schreibersite	92.28	-	91.60	-	91.54	-
Augite	3.01	$En_{48}Fs_{11}Wo_{41}$	3.07	$En_{57}Fs_{8}Wo_{35}$	3.01	$En_{49}Fs_{8}Wo_{43}$
Albite	3.54	$Ab_{93}An_{4}Or_{3}$	3.73	$Ab_{87}An_{8}Or_{5}$	4.00	$Ab_{92}An_{3}Or_{5}$
K-feldspar	0.09	$Or_{92}Ab_{7}An_{<1}$	-	-	-	-
Enstatite	0.94	$En_{79}Fs_{19}Wo_{2}$	0.50	$En_{90}Fs_{9}Wo_{1}$	0.89	$En_{77}Fs_{21}Wo_{1}$
Spinel	0.02	$(Fe_{25}Cr_{63}Mg_{12})Al_2O_4$	0.03	$(Fe_{16}Cr_{84})_3O_4$	0.10	$(Fe_{23}Cr_{77})_3O_4$
Tridymite	0.03	-	0.58	-	0.21	-
Phosphates	0.09	-	0.25	-	0.07	-

826

Figure Captions

Figure 1: (A) Photograph of the Miles meteorite showing the grain boundaries (G.B.) in the metal, the Fe-Ni metal (M) and the silicate inclusions (S.I.). **(B)** Tomogram of a portion of the Miles meteorite. The metal has been stripped away to show internal features including metal grain boundaries as grey ribbon-like features, silicate inclusions as globular masses, lobate phosphates (L.P.) as droplet-like structures extending from the silicate inclusions, and rare silicate material (S.M.) along the grain boundaries. **(C)** Map of a portion of the Miles meteorite showing metal grain boundaries (G.B.), globular silicate inclusions (S.I), lobate phosphates (L.P.), and schreibersite (Sch) concentrated along the margins of silicate inclusions and metal grain boundaries. Map is based on a reflected light microscopy image. **(D)** BSE image of a Type B silicate inclusion shown by the box in Fig. 1(C). Abbreviations are En = enstatite, Ab = albite, Chr = chrome-spinel, Ap = chlorapatite, Aug = augite, Trd = tridymite.

Figure 2: BSE Images of Type C Inclusions **(A)** Inclusion i11 with parallel elongated protrusions that extend from the margins of the inclusion into the surrounding metal (M) along which tridymite–two-feldspar lamellae are aligned. A metal grain boundary (G.B.) intersects the inclusion, along which some silicate material is visible. Schreibersite is concentrated along this grain boundary. **(B**) Detail of inclusion i11 with tridymite – K-feldspar exsolution lamellae and accessory phases enriched in incompatible elements. Radiation damage surrounds the thorium-bearing zirconolite. **(C)** Details of inclusion i11 with tridymite – two feldspar lamellae with antiperthitic and perthitic texture steeply inclined to the overall tridymite – feldspar lamellae. Accessory phases are aligned with the tridymite – feldspar lamellae. **(D)** Inclusion i29 with a micrographic texture consisting of tridymite, K-feldspar and albite. Abbreviations are M = Fe-Ni metal, G.B. = grain boundary, Sch = schreibersite, Trd = tridymite, Kfs = K-feldspar, Ab = albite, Rt = rutile, Zrc = zirconolite, Mg-Ilm = Magnesium-bearing ilmenite, Th-Zrc = thorium-bearing zirconolite, Srl = srilankite, Si-Ph = silicophosphate mineral, Bdy = baddeleyite, Mrl = merrillite.

853

854 **Figure 3:** (A) Apparent Age Spectrum (Ma), (i.e., Apparent Age (Ma) vs percentage ^{39}Ar released).
855 Two partial-plateaus are present, one at 4303 ± 6.9 Ma and one at 3496 ± 52 Ma, with gas releases
856 of 18% and 22% respectively. (B) Ca/K plot (i.e., Ca/K vs Percentage ^{39}Ar released), in the regions of
857 the partial plateaus Ca/K ratios are mostly below 1.0. (C) Arrhenius plot, where diffusion data from
858 the experiment is presented, including the Frequency Factor (D_0) and the activation energy
859 (E=kcal/mol), r=radius. Two domains have been defined:

860 (I) E = 56.04 kcal/mol $D_0/r^2 = 7.02e^{10}\ s^{-1} \pm 0.00e^{+00}$ for 20°C/Ma 0kbar closure at 218°C

861 (II) E = 66.04 kcal/mol $D_0/r^2 = 5.46e^{7}\ s^{-1} \pm 0.00e^{+00}$ for 20°C/Ma 0kbar closure at 383°C

862

863 **Figure 4: (A)** Temperature ranges for each geothermometric method: 2-feldspar = estimated
864 temperatures of equilibration for two-feldspars (Putirka, 2008); 2-pyroxene = estimated
865 temperatures of equilibration for two-pyroxenes (Putirka, 2008); Kar + Fe-m = stability range of
866 ferropseudobrookite in equilibrium with metallic iron (Simons and Woermann, 1978); disordered
867 srilankite = temperature range from which melt was rapidly cooled to form disordered srilankite
868 (Troitzsch and Ellis, 2005). (B) Temperature range over which each mineral/phase precipitates in the
869 Scheil-Gulliver cooling model (full results available in Table S4). (C) Temperature range over which
870 each mineral/phase precipitates in the equilibrium cooling model (full results available in Table S5).

871

872 **Figure 5:** Silicate inclusion composition normalized to bulk H chondrite composition of the Miles
873 meteorite bulk silicate inclusions and the partial melting experiments of synthesized H chondrite
874 starting material. Note that the Type C inclusions are most consistent with low temperatures of
875 partial melting (lowest melt fraction, F). At the highest temperatures (highest F), partial melts form
876 inclusion Types A and at moderate temperatures inclusion Type B form. A H chondrite composition
877 is included for reference.

878 * The experiments by Collinet and Grove (2020) had a higher FeO starting composition (30.80 wt.%)
879 with no metallic Fe compared to a H chondrite composition (10.30 wt.% FeO and 15.98 wt.% Fe
880 (metal); Jarosewich, 1990)
881 *Data sources:* Miles meteorite data from this study, H chondrite data from Jarosewich (1990) and
882 the results of the partial melting experiment are from Collinet and Grove (2020). Partial melting
883 experiments were conducted at range of temperatures and oxygen fugacities, with the shaded
884 region showing the overall trends and generally encompassing the range of composition observed
885 by Collinet and Grove (2020). Melt fractions (F) ranged from 28.3 at 1301°C (IW -1.77) to 5.0 at
886 1085°C (IW -1.65).
887
888 **Figure 6:** Formation model of felsic silicate inclusions in IIE iron meteorites through entrapment of
889 silicate melt inclusions in a crystallising Fe-Ni melt. (A) A melt lens forms from near-complete melting
890 of an isolated area during a transient heating event in H chondrite-like host material. Silicate and
891 metallic melts coexist as immiscible phases, however due to gravity separation the silicate droplets
892 rapidly rise to the top of the melt lens. Fe-Ni grains begin to crystallise from the melt. Heat transfer
893 away from the crystallising melt lens partially melts the adjacent parent body material, forming
894 partial melt droplets rich in silica, potassium, sodium and other incompatible elements. At lower
895 temperatures, chondrules and relict chondritic material may remain unmelted. At lower to
896 moderate temperatures, partial melts form Type C inclusions. At higher temperatures, partial melts
897 form inclusion Type A inclusions). These low-density silicate melt droplets also begin to ascend
898 through the higher density metallic melt. (B) Fe-Ni crystals in the metallic melt form nucleation
899 points from which primary γ-crystals of Fe-Ni metal grow. The remaining silicate and metal melt is
900 trapped at the junctions of these crystals. (C) The remaining silicate and metal melts crystallise,
901 forming globular silicate inclusions enriched in silica, K, Na and other incompatible elements at the
902 junctions of the Fe-Ni metal crystals. Schreibersite forms along the Fe-Ni grain boundaries and
903 adjacent to silicate inclusions through a series of redox reactions (see Section 4.3). A similar process

of impact-initiated partial melting has been proposed for the IAB iron meteorite Sombrerete (Ruzicka et al., 2006).

Figure 7: Comparison of radiometric ages of IIE iron meteorites and the possibly related Mont Dieu meteorite (iron, ungrouped), separated into metal-only, those with chondritic inclusions, and those with felsic/intermediate silicate inclusions. The fields show age clusters at ~4.2-4.7 Ga and ~3.4-3.8 Ga. Data used in this figure is available in the Supplementary Material, Table S3. Data obtained from the following sources: Miles Pb-Pb and Ar-Ar (this work); Miles, Colomera, Techado and Watson 001 Ar-Ar (Bogard et al., 2000); Miles, Watson 001 and Weekeroo Station Sm-Nd (Snyder et al., 2001); Colomera and Weekeroo Station Rb-Sr (Burnett and Wasserburg, 1967a); Colomera Rb-Sr (Sanz et al., 1970 recalculated by Bogard et al., 2000); Kodaikanal Rb-Sr (Burnett and Wasserburg, 1967b recalculated by Bogard et al., 2000); Kodaikanal Pb-Pb and U-Pb (Göpel et al., 1985); Kodaikanal Ar-Ar and Weekeroo Station K-Ar (Bogard et al., 1967); Kodaikanal K-Ar (Bogard et al., 1969); Kodaikanal Re-Os (Birck and Allègre, 1998); Tarahumara Ar-Ar (Takeda et al., 2003); Weekeroo Station Pb-Pb (Li et al., 2021); Weekeroo Station Rb-Sr (Evensen et al., 1979); Weekeroo Station and Netschaëvo Ar-Ar (Niemeyer, 1980); Mont Dieu Ar-Ar (Van Roosbroek et al., 2015); Techado K-Ar (Casanova et al., 1995); Watson 001 K-Ar (Olsen et al., 1994), Miles, Colomera, Kodaikanal, Tarahumara, Weekeroo Station, Watson 001, Mont Dieu, Arlington, and Barranca Blanca Hf-W (Kruijer and Kleine, 2019); Miles and Watson 001 Hf-W (Markowski et al., 2006); Weekeroo Station Hf-W (Schersten et al., 2006); Weekeroo Station Hf-W (Schulz et al., 2012); Weekeroo Station I-Xe (Niemeyer, 1980); Watson 001 and Arlington Hf-W (Qin et al., 2008).

Figure 8: (A): Schematic cross-section of part of the hypothesized impact crater with melt lenses and dikes that formed the IIE irons and related meteorites. B – F: (boxes are 5cm across) Examples of the textures that are posited to form in various regions of the impact crater/melt pool shown in cross-

929 section. G-K (boxes are ~2 cm across) Examples of meteorites that may represent the textures
930 shown in B-F.
931 B: Unmelted porous H chondrite-like material. C: H chondrite-like clasts within metal veins. D: Metal
932 containing chondritic clasts that show differing degrees of thermal metamorphism. E: Silicate-free IIE
933 iron meteorites. F: Metal with intermediate to felsic silicates, such as those seen in Miles, Weekeroo
934 Station,. In general, the peak temperature experienced during the impact event and the subsequent
935 thermal alteration increases from B to F.
936 G: Gilgoin H5 chondrite – an ordinary chondrite high in iron that may be similar to the parent body
937 material. H: Netschaëvo IIE iron meteorite containing angular chondritic clasts in Fe-Ni metal. I:
938 Techado IIE iron meteorite containing thermally altered H-chondrite like clasts (photo from Bogard
939 et al. (2000)). J: Miles IIE iron meteorite with globular intermediate to felsic silicate inclusions. K:
940 Arlington IIE iron meteorite which is entirely metal and contains no silicate inclusions (photo from
941 Wasson (2017)).
942 Note, these melt lenses and dikes could form in a number of crater morphologies.

(A)

G.B.

5 cm

M

S.I.

(B)

G.B.

S.I.

L.P.

S.M.

5 mm

(C)

5 mm

L.P.

G.B.

S.I.

M

Sch

(D)

Ap

En

En

Aug

Ap

Ab

M

Chr

Ab

Aug

Ap

Trd

1 mm

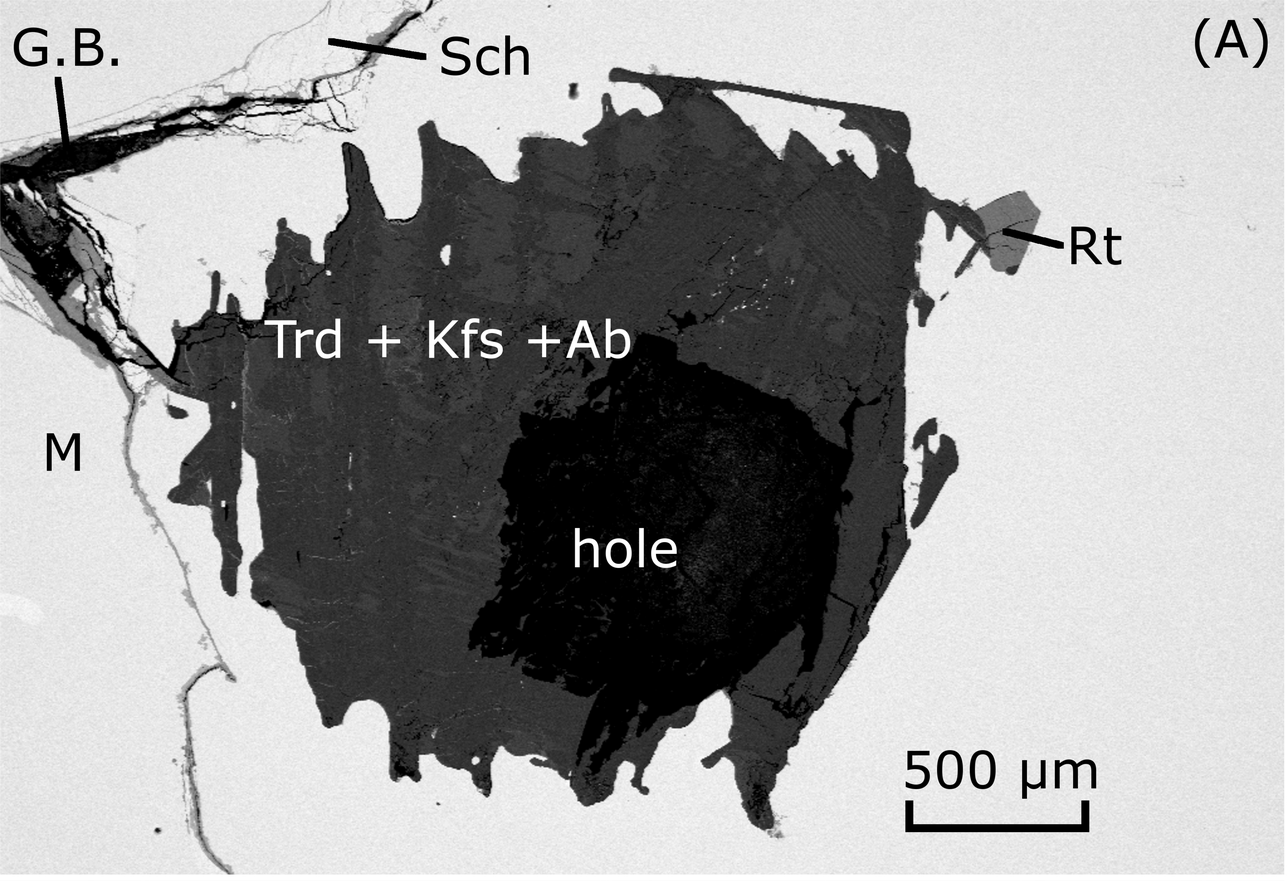
G.B.
Sch
(A)
Rt
Trd + Kfs +Ab
M
hole
500 µm

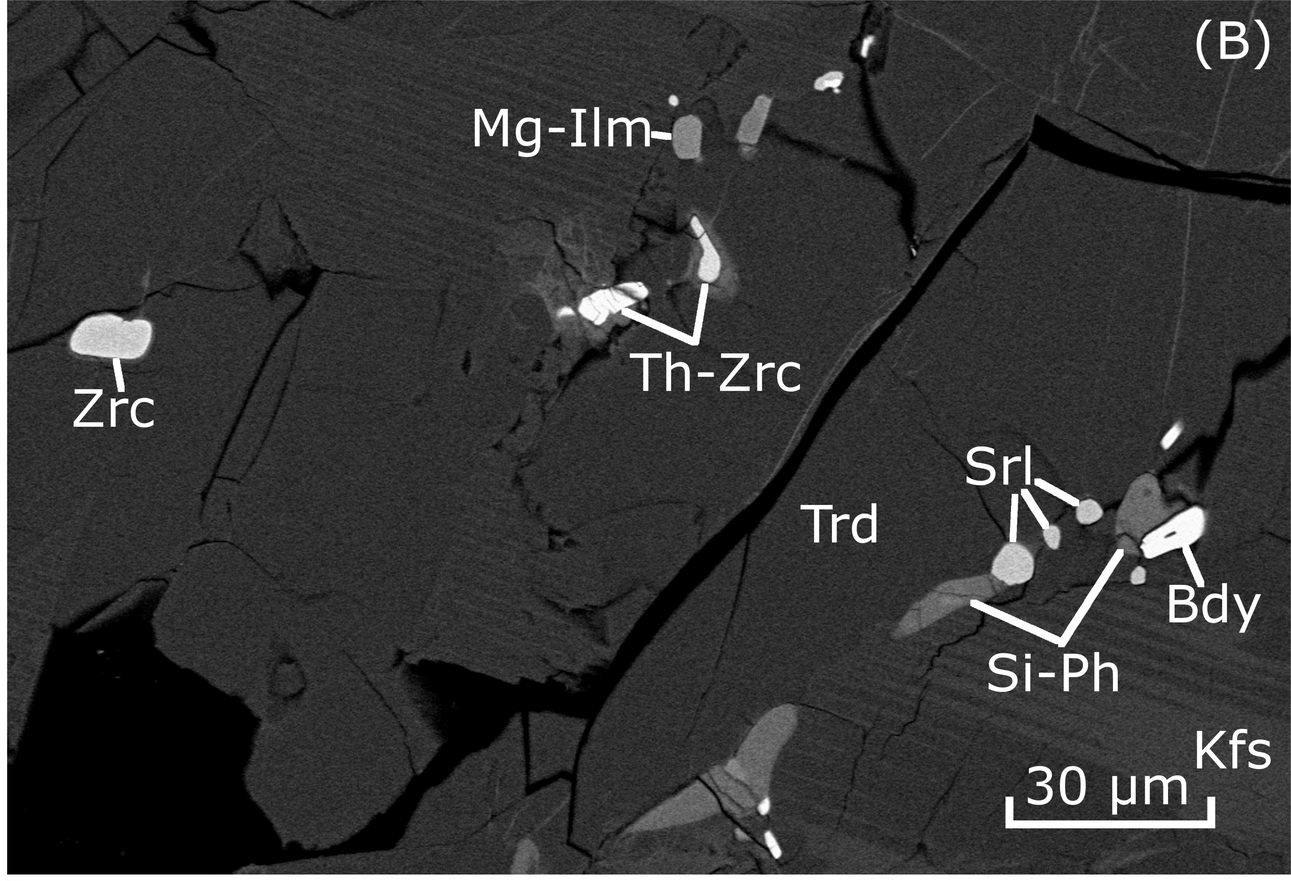
(B)
Mg-Ilm
Th-Zrc
Zrc
Srl
Trd
Bdy
Si-Ph
Kfs
30 µm

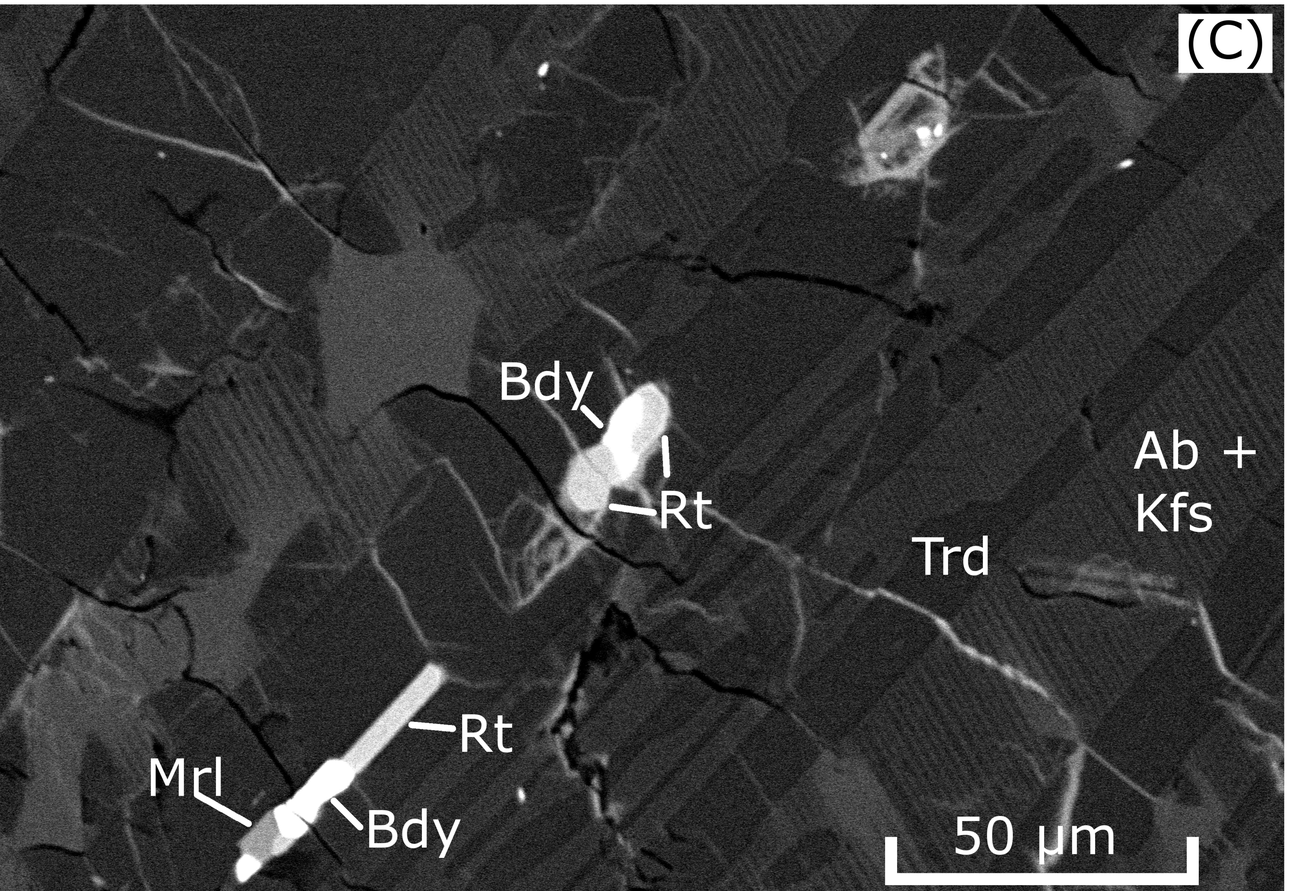
(C)
Bdy
Rt
Ab +
Kfs
Trd
Rt
Mrl
Bdy
50 µm

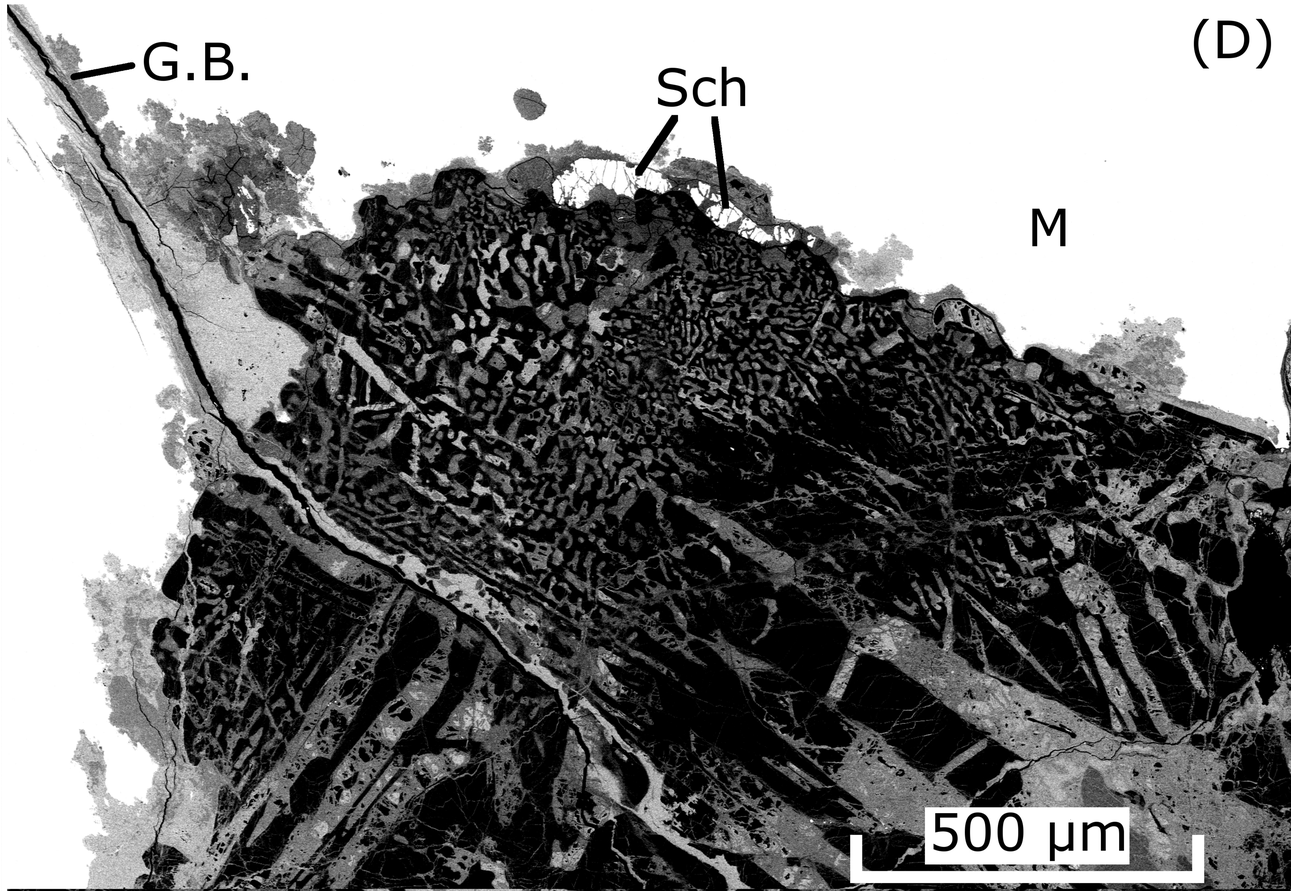
G.B.
Sch
(D)
M
500 µm

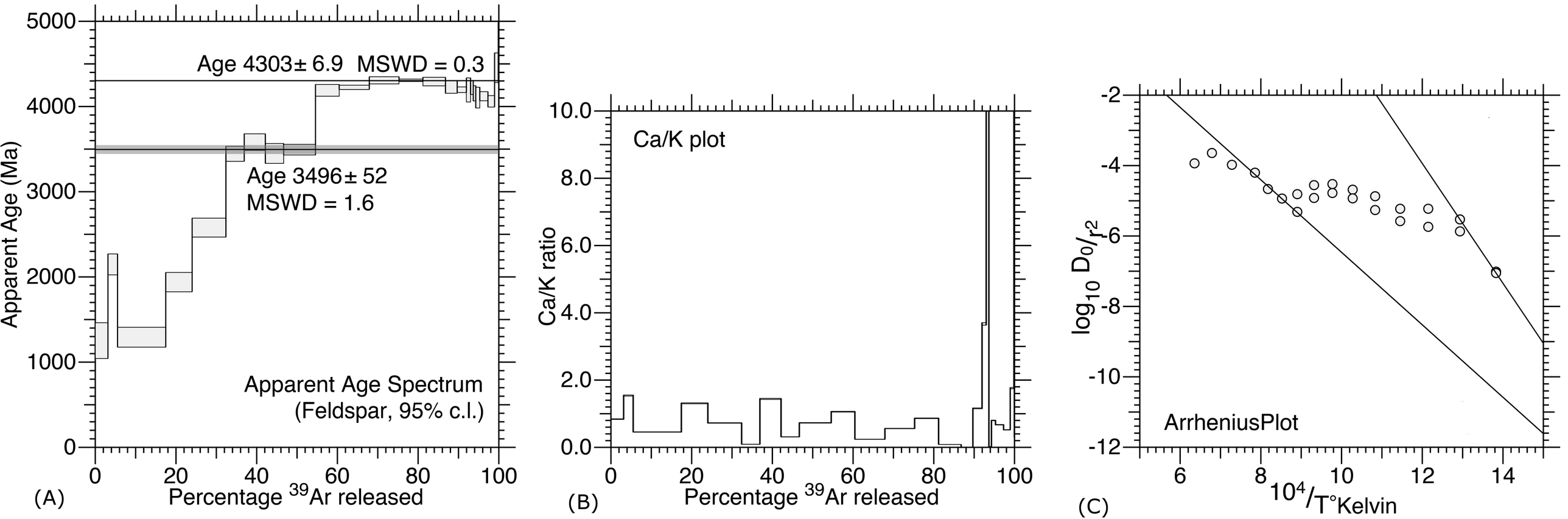
Age 4303± 6.9 MSWD = 0.3
Age 3496± 52
MSWD = 1.6
Apparent Age Spectrum
(Feldspar, 95% c.l.)
Apparent Age (Ma)
Percentage 39Ar released
(A)
Ca/K plot
Ca/K ratio
Percentage 39Ar released
(B)
ArrheniusPlot
log10 D0/r2
10^4/T°Kelvin
(C)

(A) Geothermometry

2-feldspar

2-pyroxene

Kar + Fe-m

disordered srilankite

tridymite stability

(B) Scheil-Gulliver cooling model

metal

augite

albite

spinel

enstatite

phosphates

(C) Equilibrium cooling model

metal

augite

albite

spinel

enstatite

phosphates

650 850 1050 1250 1450

Temperature (°C)

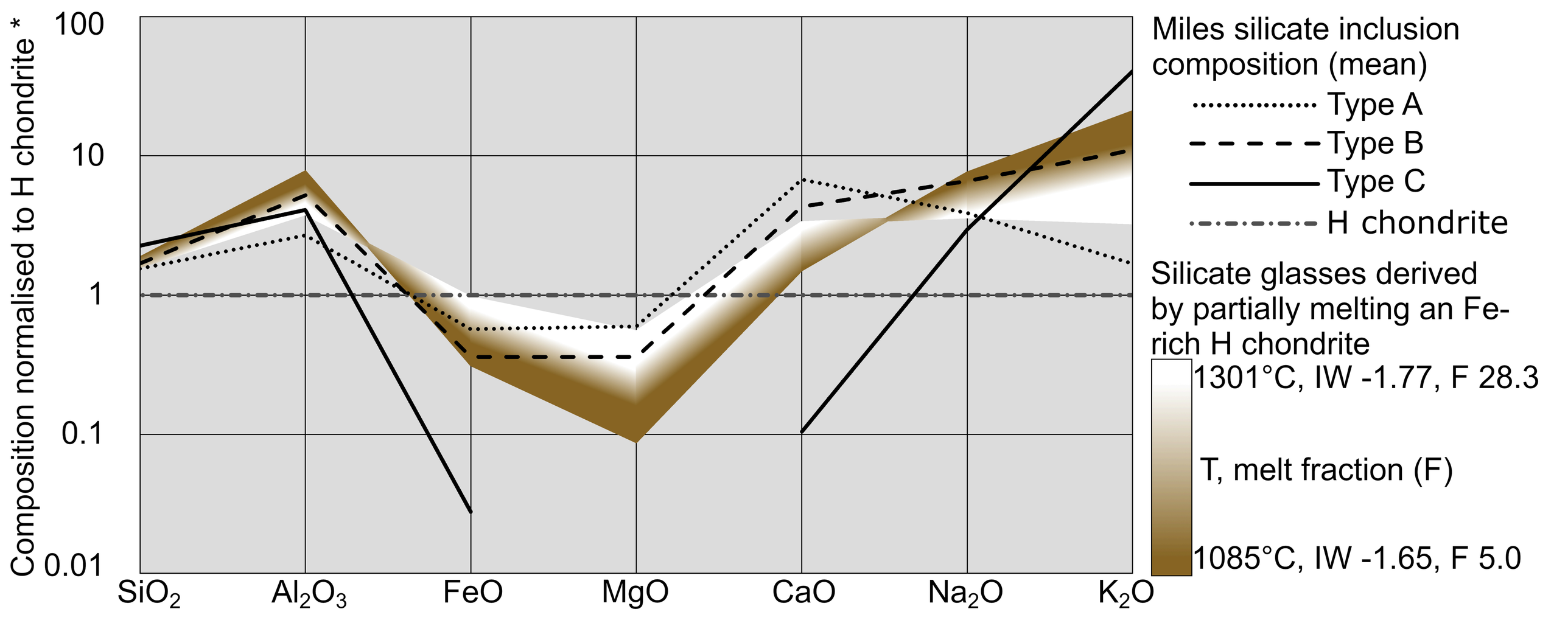
Composition normalised to H chondrite *
100
10
1
0.1
0.01
SiO2
Al2O3
FeO
MgO
CaO
Na2O
K2O
Miles silicate inclusion composition (mean)
Type A
Type B
Type C
H chondrite
Silicate glasses derived by partially melting an Fe-rich H chondrite
1301°C, IW -1.77, F 28.3
T, melt fraction (F)
1085°C, IW -1.65, F 5.0

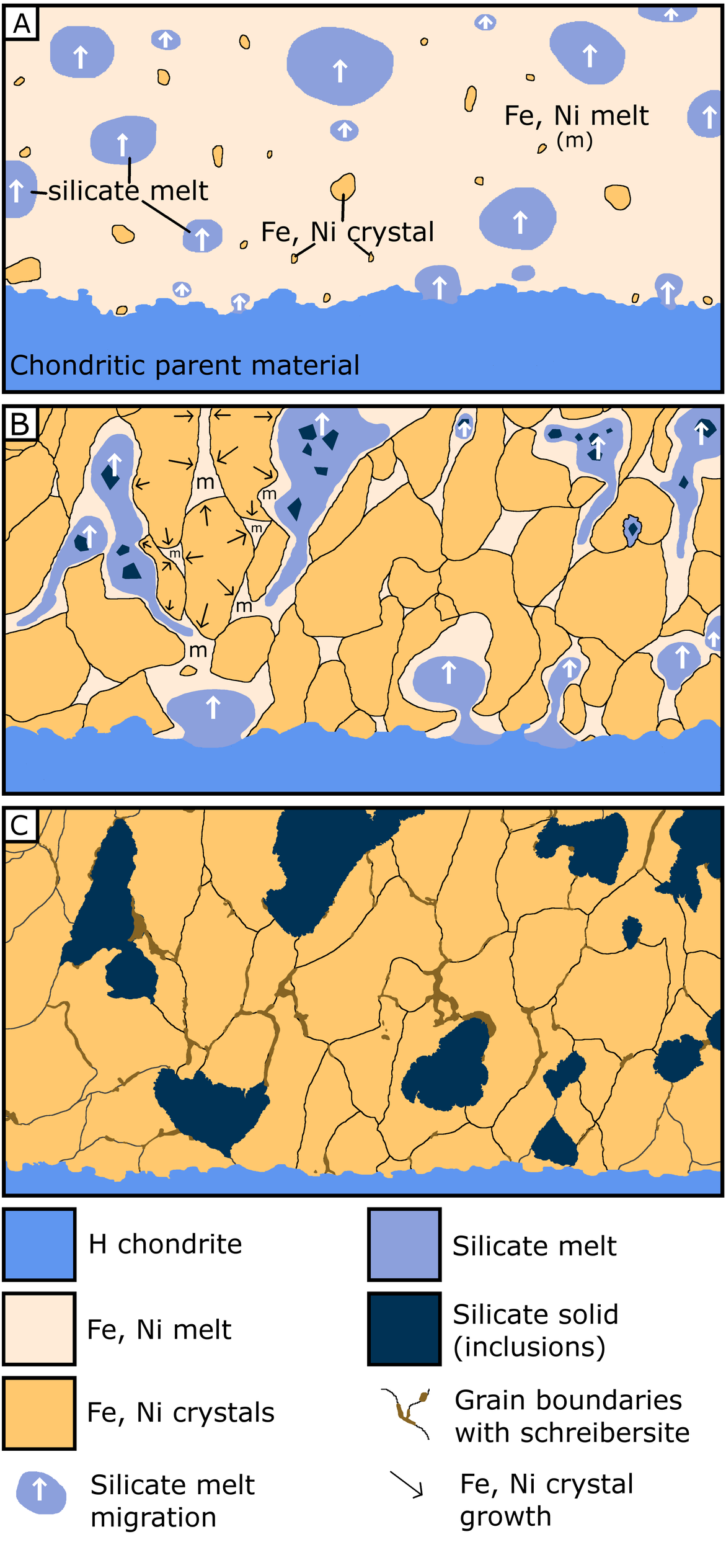
A
Fe, Ni melt
(m)
silicate melt
Fe, Ni crystal
Chondritic parent material
B
m
m
m
m
m
m
C
H chondrite
Silicate melt
Fe, Ni melt
Silicate solid
(inclusions)
Fe, Ni crystals
Grain boundaries
with schreibersite
Silicate melt
migration
Fe, Ni crystal
growth

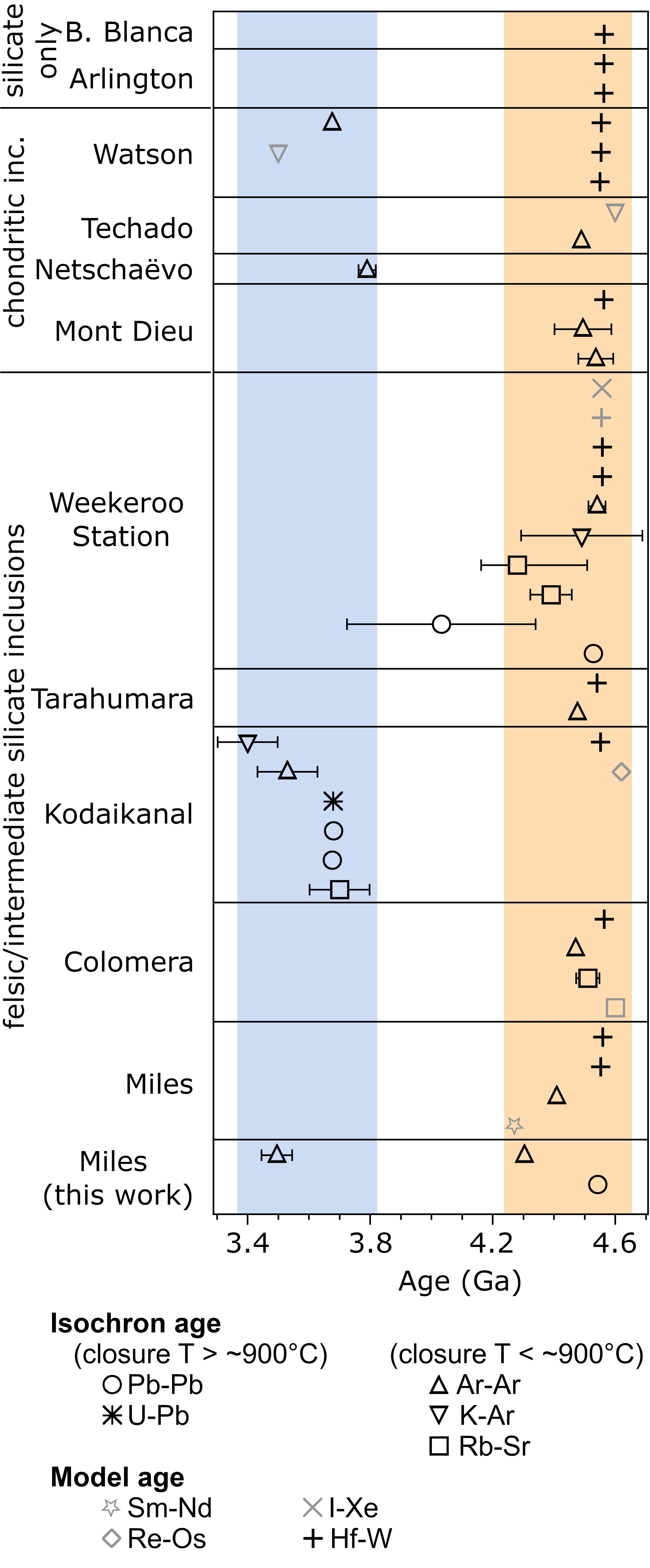
silicate only
B. Blanca
Arlington
chondritic inc.
Watson
Techado
Netschaëvo
Mont Dieu
felsic/intermediate silicate inclusions
Weekeroo Station
Tarahumara
Kodaikanal
Colomera
Miles
Miles (this work)
3.4
3.8
4.2
4.6
Age (Ga)
Isochron age
(closure T > ~900°C)
Pb-Pb
U-Pb
(closure T < ~900°C)
Ar-Ar
K-Ar
Rb-Sr
Model age
Sm-Nd
I-Xe
Re-Os
Hf-W

Crater Rim

lithic breccias

Impact Crater

fallback breccia

melt lenses

vein networks

intrusive Fe,Ni melt dikes

monomictly brecciated basement

(A)

Peak temperature, increasing thermal alteration

(B) Unmelted porous H chondrite-like material

(C) H chondrite-like clasts within metal veins

(D) Metal with alterered H chondrite-like clasts

(E) Metal with intermediate to felsic silicates

(F) Silicate-free metal

5cm (B)-(F)

~1cm (G)-(K)

H chondrite-like material

lithic breccia

fallback breccia

Fe,Ni-metal

"felsic" silicates

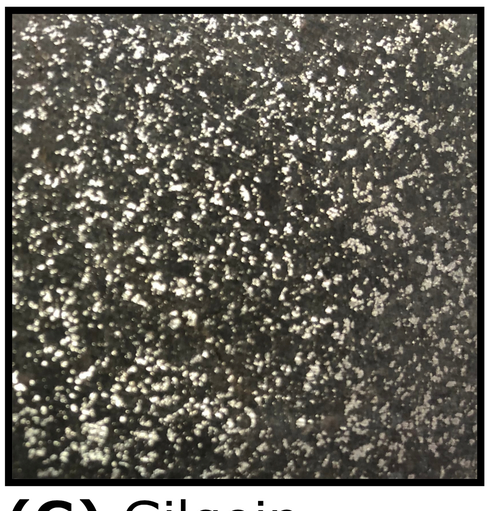

(G) Gilgoin (H5 chondrite)

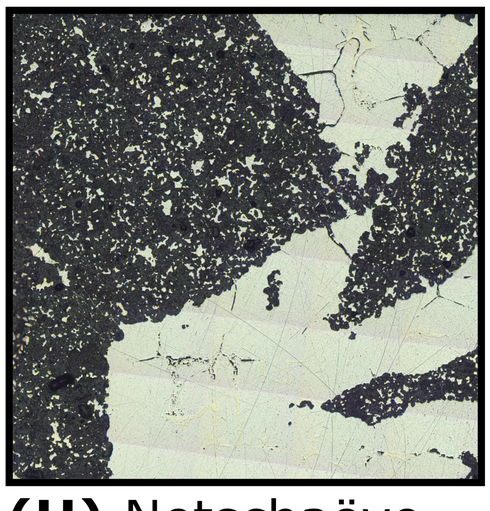

(H) Netschaëvo (IIE iron)

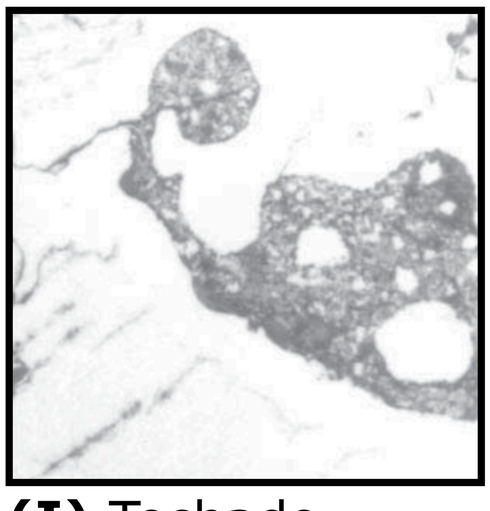

(I) Techado (IIE iron)

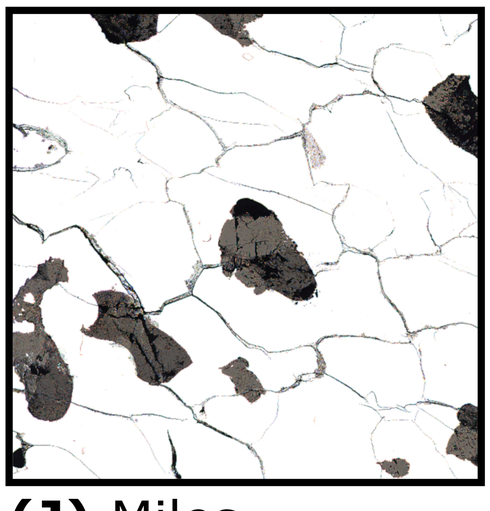

(J) Miles (IIE iron)

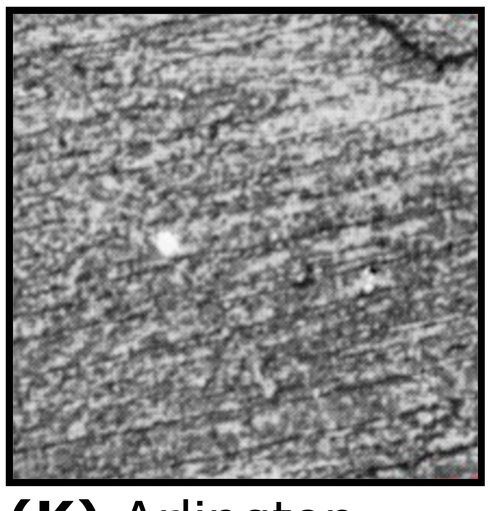

(K) Arlington (IIE iron)